



A11104 023377

NIST
PUBLICATIONS

NISTIR 5226

Penetration of Proton Beams Through Water I. Depth-dose Distribution, Spectra and LET Distribution

Martin J. Berger

U.S. DEPARTMENT OF COMMERCE
Technology Administration
National Institute of Standards
and Technology
Physics Laboratory
Ionizing Radiation Division
Gaithersburg, MD 20899

Prepared for:

National Cancer Institute
Bethesda, MD 20892

~~QC~~
100
.U56
#5226
1993

NIST

DATE DUE

AUG 25 2003	7983509	16721
GAYLORD		PRINTED IN U.S.A.

**NATIONAL INSTITUTE OF STANDARDS
AND TECHNOLOGY**
Arati Prabhakar, Director

Penetration of Proton Beams Through Water

I. Depth-dose Distributions, Spectra and LET Distributions

Martin J. Berger*

Physics Laboratory**
National Institute of Standards and Technology
Gaithersburg, MD 20899

The penetration of protons through a water phantom was calculated with the Monte Carlo program PTRAN, which takes into account energy-loss straggling, multiple scattering, and nonelastic nuclear interactions. Calculations were done for incident proton beams incident with energies between 250 MeV and 50 MeV. The information obtained includes depth-dose curves as well as energy spectra of primary protons at various depth. Good agreement was found between calculated and measured relative depth-dose distributions, except at extreme depths. A systematic tabulation was made of various parameters that characterize the shape of the Bragg peak. The energy spectra were used to obtain LET distributions for primary protons. In addition, dose-averaged LET-values were obtained which include contributions from primary protons as well as from secondary charged particles produced in nuclear reactions.

*Work carried out for the National Institute of Standards and Technology under contract 50SBN2C7042.

**Ionizing Radiation Division, Technology Administration, U.S. Department of Commerce, Gaithersburg, MD 20899

1. Introduction

In a previous report (Berger, 1993a) a Monte Carlo program called PTRAN was presented which calculates the penetration, diffusion and slowing down of protons in extended media. The present report describes results obtained with PTRAN that are relevant to proton dosimetry and treatment planning. The results include (a) depth-dose distributions in water, and (b) proton energy spectra and LET distributions as functions of the depth in the phantom, for monoenergetic proton beams incident with energies from 50 MeV to 250 MeV, and for beams incident with a Gaussian energy spectra. A third report, now being prepared, will deal with three-dimensional dose distributions.

The calculations described in this report pertain to a proton beam incident perpendicularly onto a semi-infinite homogeneous water phantom, occupying the region $z \geq 0$. Unless the contrary is stated, all results shown are normalized to one incident proton. In setting up the calculations and in presenting the results, it was found useful to introduce a scaled depth-variable z/r_0 , where r_0 is the CSDA range at the incident-beam energy T_0 . Thereby the explicit dependence of the results on T_0 is reduced, which facilitates interpolation.

The CSDA range r_0 is a path length calculated in the continuous-slowing-down approximation, by integrating the reciprocal of the stopping power with respect to energy, from the initial energy T_0 down to zero. The required stopping powers were obtained with the computer program PSTAR (Berger, 1993b) which produces results equivalent to those in a forthcoming ICRU Report 49 (ICRU, 1993). Stopping powers and ranges for protons in water are shown in table 1, at energies needed to interpret the results in this report.

2. Track Length per Unit Depth

Let dt/dz denote the average proton track length per unit depth, at depth z . Without nonelastic nuclear reactions, and without energy-loss straggling and multiple scattering, dt/dz would simply be equal to unity for all depths smaller than r_0 , and would drop to zero abruptly at r_0 . Results from PTRAN are shown in figures 1a and 1b, in the form of plots of dt/dz vs. z/r_0 , for beams with initial energies from 50 MeV to 250 MeV. At depths smaller than the CSDA range, dt/dz decreases gradually in an almost linear fashion, due to the removal of protons from the beam by nonelastic nuclear interactions. At depths near and beyond r_0 , where nuclear interactions are unimportant, dt/dz decreases rapidly, mainly due to the effects of energy-loss straggling.

3. Average Energy Loss of the Primary Proton Beam As Function of Depth

The two quantities of interest are: $(dE/dz)_c$, the energy lost from the proton beam per unit depth at depth z , due to Coulomb interactions with electrons of the target atoms; and $(dE/dz)_n$, the energy loss per unit depth at depth z due to nonelastic nuclear interactions. Both of these quantities are plotted in figure 2 for the case of an incident 160-MeV beam.

Figure 3 describes the results of a model study for an 160-MeV beam. Three curves of $(dE/dz)_c$ vs. the scaled depth z/r_0 are shown, obtained under the following conditions: (a) by a complete treatment, including energy-loss straggling and multiple-scattering deflections; (b) with energy-loss straggling disregarded; (c) with multiple-scattering deflections disregarded. For depths less than about $0.9 r_0$ the three curves are close to each other, which implies that $(dE/dz)_c$ in this depth region is largely determined by the range-energy relation and by the nonelastic nuclear cross section. At greater depths straggling is increasingly important, and reduces the height of the Bragg peak. Multiple-scattering angular deflections, on the other hand, have little influence on $(dE/dz)_c$, and are important only for radial dose distributions.

Curves of $(dE/dz)_c$ vs. z/r_0 are shown in figure 4, and curves of $(dE/dz)_n$ vs. z/r_0 in figure 5, for monoenergetic beams with energy $T_0 = 250, 200, 160, 130, 100, 70$ or 50 MeV. The residual dependence of these scaled results on T_0 is small, so that interpolation with respect to T_0 is feasible. In order to further increase the accuracy of such interpolations, similar results were generated for 25 values of T_0 between 250 MeV and 50 MeV. The list of these beam energies is the same as the set of energies in table 1.

4. Depth-Dose Curves

The energy lost by primary protons in Coulomb collisions is mostly transferred to secondary electrons; to a lesser extent it is used for molecular excitation and dissociation. As shown in table 2, the ranges of the secondary electrons from proton-impact ionization events are much smaller than the ranges of the primary protons. Energy transport by secondary electrons therefore has little effect on depth-dose curves, except in a very thin transition region near the entrance face of the phantom. In the present work energy transport by secondary electrons was disregarded. A calculation is in progress, however, of the slowing down of the secondary electrons, because the electron energy degradation spectra are of interest in radiation chemistry and biology.

Most of the energy lost by primary protons in nuclear reactions is transferred to secondary charged particles (protons, deuterons, alpha particles, heavy recoil nuclei), neutrons, and gamma rays. Seltzer (1993) recently estimated the number and energy spectra of secondary charged particles and neutrons from nonelastic reactions of protons with ^{16}O , using an intranuclear-cascade computer code of Brenner and Prael (1989). The emission of gamma-rays was found to be unimportant. The fraction of the primary proton energy transferred to secondary charged particles, per nuclear collision, is almost 70% at 250 MeV and decreases to 30% at 10 MeV. Seltzer's results for this fraction, at 15 primary-proton energies, are plotted in figure 6. Combining these results with the spectrum of primary protons as a function of depth (obtained with PTRAN), one can obtain the depth-dependent fraction $a(T_0, z)$ of $(dE/dz)_n$ that is transferred to secondary charged particles. This fraction is shown in table 3 as a function of T_0 and the scaled depth z/r_0 .

Energy is transferred to secondary neutrons at a rate equal to $[1-a(T_0, z)](dE/dz)_n$. These neutrons are more penetrating than the primary protons, and therefore make only a small contribution to the dose at the depths $z \leq 1.04 r_0$ to which the primary protons can penetrate. This was shown, for example, by transport calculations of Alsmiller (1967). A predominant share of the energy transferred to secondary charged particles is imparted to secondary protons. In reactions of protons with ^{16}O nuclei, this share, according to Seltzer (1993) is 93%, 81%, 65%, 53% or 46%, respectively, for primary-proton energies of 200, 100, 50, 25 or 10 MeV.

Secondary particles heavier than protons have short ranges, and one can assume that they are absorbed "locally," i.e., that their energy is imparted to the medium very close to the point where they originate. The ranges of the secondary protons, however, are not necessarily very small compared to the ranges of the primary protons. However, the effect of energy transport by secondary protons is expected to be small. Whereas the amount of energy imparted to the medium at any point is decreased due to the emigration of secondary protons towards greater depths, there is also a compensating increase due the immigration of secondary protons coming from smaller depths. The two effects will to a considerable extent cancel each other, because the rate of production of secondary protons (and their emission spectrum) vary slowly with depth (except near the Bragg peak where nuclear interactions are in any case rare). In the present work, the simplifying assumption was therefore made that the energy from all secondary charged particles, including protons, is absorbed "locally." As will be shown in Section 5, this approximation appears justified by the fairly good agreement between calculated and measured depth-dose distributions.

The rate of energy deposition per unit depth, dD/dz , was thus calculated as the sum $(dE/dz)_c + a(T_0, z)(dE/dz)_n$. Figure 7 compares a depth-dose distribution calculated in this manner, with a corresponding distribution calculated with neglect of nonelastic nuclear reactions. It can be seen that the nuclear interactions bring about an increase of the dose at shallow depths, and a decrease at large depths, specially around the Bragg peak. In figure 8, the relative contribution to the total absorbed dose from secondary charged particles is shown as a function of the scaled depth z/r_0 , for seven beam energies between 250 MeV and 50 MeV. Depth dose distributions for the same set of beam energies are shown in figures 9a and 9b.

In figures 10a and 10b depth-dose distributions are plotted for beams with a Gaussian spectrum, with a mean energy $\langle T_0 \rangle_{av} = 160$ MeV and with various assumed standard deviations up to 2% of $\langle T_0 \rangle_{av}$. These results were obtained by interpolation in the database for 25 monoenergetic beam energies. The Gaussian beam spectra were actually truncated so as to include only energies that differ from the mean energy by up to four times the standard deviation. It can be seen in these figures that the ratio of the height of the Bragg peak to the entrance dose depends sensitively on the standard deviation of the Gaussian beam spectrum.

The shape of the Bragg peak can be characterized in terms of various parameters, which are illustrated in figure 11 for the case of a 70-MeV beam. These parameters include the peak dose, D_m , the depth z_m where the dose peaks, and the depths z_{80} and z_{50} beyond the Bragg peak where the dose is equal to

80%, respectively 50%, of the peak dose, and the corresponding widths w_{80} and w_{50} of the depth-dose curve at the 80% and 50% levels. Another quantity of interest is the extrapolated range r_x , which is determined as follows. A point on the depth-dose curve (beyond the Bragg peak) is found where the slope of the depth-dose curve has a maximum. A straight line with the same slope is drawn through this point. The extrapolated range r_x is equal to the depth at which the line intersects the z-axis. All of the above parameters were evaluated for seven beam energies between 240 MeV and 50 MeV, and are given in table 4. Included in this table are not only results for monoenergetic beams, but also results for beams with a Gaussian spectra (again truncated at four standard deviations), with standard deviations equal to 0.0, 0.5, 1, 1.5 and 2% of the mean energy.

5. Comparisons of Calculated and Measured Depth-Dose Curves

Comparisons were made with depth-dose curves measured at the University of Uppsala (Larsson, 1961), at the Harvard Cyclotron Laboratory (Gottschalk, 1991), and at the Paul-Scherrer Institute (Scheib and Pedroni, 1991). The experimental depth-dose curves are only relative. In the comparisons, the calculated and experimental curves were therefore both normalized to unit height at peak of the depth-dose distribution. The experimenters provided estimates of the mean energy of their beams, but the shape of the beam spectrum is not known. In the comparisons made here, it is assumed that the shape is Gaussian. The mean energy and standard deviation of beam spectrum used in the calculation were chosen so as to obtain good agreement with the experimental curves, especially in the regions around the Bragg peak where the dose is no smaller than 80% of the peak value.

Authors	Mean Beam Energy Estimated by Experimenter	Mean Beam Energy and Percent Standard Deviation Assumed in Calculation	
Gottschalk et al.	158.6 MeV	158.5 MeV,	0.95%
Larsson	187 MeV	188.4 MeV,	0.5%
Scheib and Pedroni	214.3 MeV	214.5 MeV,	0.4%

The comparisons with the three experiments are shown in figures 12, 13, and 14, respectively. The calculated results are represented by solid curves, and the experimental results by points(o). In figure 12, these points actually represent base points which - when fitted by a cubic spline - accurately represent the experimental depth-dose curve. The percent differences between the measured and calculated depth-dose values are listed in tables 5, 6, and 7. The differences amount to only a few percent at depths up to and somewhat beyond the Bragg peak. This indicates that the assumption of a "local absorption" of energy from secondary charged particles does not introduce serious errors.

At very great depths beyond the Bragg peak the experimental depth-dose values fall significantly below the calculated values, and these differences

increase with depth. These discrepancies are difficult to understand from a theoretical standpoint. Nuclear interactions play no role at these depths. There is some uncertainty in regard to the best choice of the mean excitation energy for water, which in turn affects the CSDA range. Bichsel and Hiraoka (1992) suggested that the mean excitation energy of water is 79.8 eV rather than 75 eV as assumed in the present work. This would increase the CSDA ranges at energies in the energy region of interest by approximately 0.8%, and would make the discrepancies even larger. The assumption of a Gaussian shape for the beam spectrum is probably not justified for the tails of the spectrum. However, trial calculations with a Gaussian distribution truncated at two standard deviations, and with a parabolic beam spectrum with the same standard deviation, reduced the depth-dose at very great depths only slightly, not enough to decrease the discrepancies significantly. It may be the case that at very great depths, where the depth-dose curves falls steeply and the residual proton ranges are very short, the detectors (small ionization chambers) can no longer be considered to be thin, and the effective depth assigned to the measurement points may be in error.

6. Energy Spectra

Let $y(T,z)dT$ denote the average proton track length (per unit depth) at depth z , for protons with energies between T and dT . Note that by integrating $y(T,z)$ with respect to T one obtains the track length dt/dz discussed in Section 2.

It is convenient to summarize the shape of the spectra in terms of the average energy

$$T_{av} = \frac{\int T y(T,z) dT}{\int y(T,z) dT}, \quad (1)$$

and the standard deviation

$$\sigma_T = \frac{\int (T-T_{av})^2 y(T,z) dT}{\int y(T,z) dT}. \quad (2)$$

T_{av} and σ_T are plotted in as figure 15 as functions of z/r_0 for the case of an 160-MeV beam. The standard deviation rises with increasing depth, until a maximum is reached at a depth slightly smaller than r_0 , and then rapidly decreases.

The spectral histograms obtained with PTRAN were converted to spectral curves by a cubic-spline least-squares smoothing routine. Smoothed energy spectra are shown in figure 16a for small and intermediate depths, and in figure 16b for great depths (near and beyond the Bragg peak). Results for two beam energies (160 MeV and 70 MeV) are shown together. The spectra were scaled by plotting the quantity $T_0 y(T,z)$ vs. T/T_0 , for a selected set of scaled depths z/r_0 . The shapes of the scaled spectra at the two beam energies are quite similar, and the residual dependence on T_0 is slight.

Except at depths that are either very small or very large compared to the CSDA range, the primary proton spectra are almost symmetric and have a shape close to a Gaussian distribution. The departures from a Gaussian distribution can be exhibited by plotting the spectral histograms as functions of the reduced variable $(T - T_{av})/\sigma_T$, and comparing them with a Gaussian distribution with mean zero and unit standard deviation. The results of this comparison are shown in figure 17a for small and intermediate depths, and in figure 17b for great depths. The spectra are slightly skewed and depart from a Gaussian at a depth $z = 0.1 r_0$, and very slightly also at $z = 0.2 r_0$; at depths up to $z = 0.9 r_0$ the differences are then practically negligible; at even greater depths the spectra are again skewed and depart significantly from a Gaussian. The departures of the spectra from a Gaussian shape are important for some applications, for example the analysis of proton range measurements to obtain mean excitation energies (see, e.g., Bichsel and Hiraoka, 1992). For other purposes such as the calculation of the source spectrum of secondary electrons, it would be sufficiently accurate to use a Gaussian distribution with a mean value and standard deviation obtained from PTRAN.

The output from PTRAN provides proton energy spectra only for spectra energies T down to a cut-off energy which was chosen to 0.142 MeV and which cannot easily be lowered with the Monte Carlo model and cross sections used. At depths less than 95% of r_0 this restriction is unimportant because there are practically no protons in the spectrum with energies below 0.142 MeV. At greater depths, the spectra can easily be extended by extrapolation. For this purpose it is useful to plot $S(T)y(T,z)$, where $S(T)$ is the proton stopping power. As can be seen in the illustrative plots in figure 18 for an 160-MeV beam, at depths greater than $0.95 r_0$ the product $S(T)y(T,z)$ is practically independent of T at very low energies, a result which is anticipated from the theory of energy slowing-down spectra. Therefore the proton spectra can easily be extrapolated to arbitrarily low energies.

In practice, proton beams with different intensities and ranges are often combined to achieve a uniform dose over large depth intervals. This was done, for example, by Koehler et al. (1975) using a rotating wheel with different thicknesses of plastic sheet. It is of interest to determine the proton spectra that correspond to such spread-out dose distributions, which can be easily accomplished using results from PTRAN. Figure 19a shows a calculated spread-out depth dose curve (solid curve) and compares it with the Bragg curve for a monoenergetic 160-MeV beam (dotted curve). The vertical lines indicate the positions of the Bragg peaks and the intensities of the many contributing monoenergetic proton beams. The corresponding proton spectra for the spread-out dose distribution are shown in figure 19b.

7. LET Distributions and Mean Values

The spectrum weighted with the stopping power, $S(T)y(T,z)$, can be converted to an LET distribution, by changing from the variable T to the variable L (linear energy transfer, numerically equal to the stopping power). One thus obtains the distribution $\phi(L,z)$ which is defined so that $\phi(L,z)dL$ represents the contribution to the dose due from particles with LET-values between L and $L + dL$.

LET distributions are shown in figure 20 at four depths for the case of an incident 160-MeV beam. These results include contributions from primary protons only, and illustrate the shift of the LET distributions to higher LET values with increasing depth. In the region of the Bragg peak the LET values are large enough so that one would expect an enhanced biological effectiveness per unit dose.

For a rapid survey of radiation quality it is of interest to consider average LET values as functions of depth. The contribution to the dose-averaged LET from primary protons can be calculated from the expression

$$\langle \text{LET} \rangle_d = \frac{\int S^2(T) y(T, z) dT}{\int S(T) y(T, z) dT} \quad (3)$$

In the evaluation of this expression, $y(T, z)$ can be extrapolated, if necessary, to energies below 0.142 MeV, as indicated in Section 7. In order to include the contributions from secondary charged particles released in nuclear reactions, eq (3) must be generalized to

$$\langle \text{LET} \rangle_d = \frac{\sum_j \int S_j^2(T) y_j(T, z) dT}{\sum_j \int S_j(T) y_j(T, z) dT} \quad (4)$$

where the index $j = 0$ pertains to primary protons, and $j = 1, 2, \dots$ to secondary protons, alpha particles, etc. The required spectra of the secondary particles are available from the calculations of Seltzer(1993) with the intranuclear-cascade code of Brenner and Prael (1989). The stopping powers for protons and alpha particles were taken from Berger(1993) and those for heavier particles from the TRIM program of Ziegler (1990).

Figures 21a and 21b show the dose-averaged LET for a beam energies of 160 MeV and 70 MeV. The dotted curves represent the contributions from primary protons only, and the solid curves take into account the contributions from primary protons and all secondary charged particles. It can be seen that at depths up to $0.95 r_0$ the contribution from secondary charged particles significantly increases the dose-averaged LET, but that $\langle \text{LET} \rangle_d$ in this region has values no greater than about 4 keV/ μm . By contrast, the dose-averaged LET at depths greater than $0.95 r_0$ becomes as great as 15 keV/ μm at 160 MeV, and 24 keV/ μm at 70 MeV. These large values are due almost entirely to the contribution from primary protons.

Figure 22 shows a family of curves of total $\langle \text{LET} \rangle_d$ vs. z/r_0 for monoenergetic beams with energies between 250 MeV and 50 MeV. These results include the contributions from primary protons and all secondary charged particles. The lower the beam energy, the greater are the values of $\langle \text{LET} \rangle_d$ at depths near and beyond the Bragg peak. This is shown in more detail in the inset in figure 22.

It is of interest to have corresponding results for spread-out Bragg peaks obtained by the combination of many different beams with various energies and intensities. Such results are shown in figures 23a and 23b for

beams with maximum energies of 160 MeV and 50 MeV, respectively. The left-hand panels in these figures show the spread-out dose distributions and the Bragg peaks and intensities of the contributing beams. The right-hand panels compare curves of $\langle \text{LET} \rangle_d$ vs. z/r_0 for the spread-out dose distribution (solid curve) and from a monoenergetic beam (dotted curve).

The dose-averaged LET can serve as a rough indicator of biological effectiveness. The results shown in figures 21-23 indicate that the LET-increase due to secondary charged particles from nuclear reactions is small enough so that it can be expected to lead to only a small enhancement of biological effectiveness. The sharp rise of the dose-averaged LET at and beyond the Bragg peak, due to the presence of primary protons of very low energy, is expected to result in a more significant enhancement of the biological effectiveness. These considerations have been tentatively quantified by Seltzer (1993) with the use of a plausible relation between RBE and LET (based on a survey of experimental results). The conclusions are that the RBE may be 1 to 1.1 at shallow and intermediate depths, and as large as 1.3 to 1.5 at great depths.

References

- Berger, M. J. (1993a). Proton Monte Carlo transport program PTRAN, National Institute of Standards and Technology Report NISTIR-5113.
- Berger, M. J. (1993b). ESTAR, PSTAR and ASTAR: Computer programs for calculating stopping-power and range tables for electrons, protons and helium ions, National Institute of Standards and Technology Report NISTIR 4999.
- Bichsel, H. and Hiraoka, T. (1992). Energy loss of 70-MeV protons in elements, Nucl. Instr. Meth. B66, 345.
- Brenner, D. and Prael, R. E. (1989). Calculated differential secondary-particle production cross sections after nonelastic neutron interactions with carbon and oxygen between 15 and 60 MeV, Atomic Data and Nuclear Data Tables 41, 71-13.
- Gottschalk, B. (1991). Private communication, dated 9 December 1991.
- ICRU (1993). Stopping Powers and Ranges for Protons and Alpha Particles, Report 49, International Commission on Radiation Units and Measurements.
- Koehler, A. M., Schneider, R. J. and Sisterson, J. M. (1975). Range modulators for proton and heavy ions, Nucl. Instr. Meth. 131, 437.
- Larsson, B. (1961). Pre-therapeutic physical experiments with high energy protons, Brit. J. Radiology, 34, 143-151.
- Scheib, E. and Pedroni, E. (1991). Treatment planning for dynamic proton therapy, pp. 67-70, Proceedings of Proton Radiotherapy Workshop held at the Paul Scherrer Institute on February 28 and March 1 1991. Also private communicated from E. Pedroni, date 25 February 1992.
- Seltzer, S. M. (1993). An assessment of the role of charged secondaries from nonelastic nuclear interactions by therapy proton beams in water, National Institute of Standards and Technology Report, to be published.
- Ziegler, J. F. (1990). *TRIM-90, The Transport of Ions in Matter*. The method underlying this computer code is described in Ziegler, J. F, Biersack, J. P. and Littmark, U. (1985), *The Stopping and Range of Ions in Matter*, Pergamon Press, Elmsford, N.Y.

Table 1. Stopping powers and CSDA ranges for protons in water.

T (MeV)	dE/dx (MeV cm ² g)	r _o g/cm ²
250.0	3.910	37.94
237.5	4.032	34.79
225.0	4.169	31.74
212.5	4.320	28.80
200.0	4.491	25.96
190.0	4.642	23.77
180.0	4.810	21.65
170.0	4.997	19.614
160.0	5.207	17.653
152.5	5.381	16.237
145.0	5.573	14.867
137.5	5.784	13.546
130.0	6.018	12.275
122.5	6.280	11.055
115.0	6.574	9.888
107.5	6.907	8.775
100.0	7.286	7.718
92.5	7.723	6.718
85.0	8.233	5.777
77.5	8.834	4.897
70.0	9.555	4.080
65.0	10.121	3.572
60.0	10.775	3.093
55.0	11.539	2.644
50.0	12.443	2.227

Table 2. Comparison of the ranges of proton and secondary electrons in liquid water.

T: Proton energy
 $r_o(p)$: CSDA range of proton of energy T
 E_M : Largest possible energy transfer from proton to secondary electron
 $r_o(e)$: CSDA range of secondary electron of energy E_M

T (MeV)	E_M (MeV)	$r_o(p)$ (g/cm ²)	$r_o(e)$ (g/cm ²)	$r_o(e)/r_o(p)$
300.0	0.7580	55.24	0.3081	0.005577
250.0	0.6172	37.95	0.2352	0.006197
200.0	0.4821	25.97	0.1678	0.006463
150.0	0.3529	15.78	0.1073	0.006797
100.0	0.2295	7.721	0.05575	0.007221
80.0	0.1817	5.186	0.03848	0.007421
60.0	0.1349	3.094	0.02364	0.007641
50.0	0.1118	2.228	0.01728	0.007757
40.0	0.08900	1.489	0.01173	0.007878
30.0	0.06640	0.8856	0.007080	0.007999
20.0	0.04403	0.4260	0.003456	0.007999
10.0	0.02190	0.1229	0.001006	0.008188

Table 3. Fraction $a(T_0, z)$ of the energy lost at depth z by primary protons in nuclear reactions that is transferred to secondary charged particles. Results are for proton beams incident with energy T_0 . Depths are expressed in units of the CSDA range r_0 . Entries with dashes (---) are for beam energies and depth for which all protons have energies below the threshold for nuclear reactions with oxygen-¹⁶ nuclei.

$z \backslash r_0$	T_0 (MeV)						
	250.0	200.0	160.0	130.0	100.0	70.0	50.0
0.000	0.691	0.672	0.653	0.634	0.611	0.582	0.559
0.100	0.687	0.665	0.645	0.627	0.605	0.579	0.557
0.200	0.680	0.659	0.639	0.621	0.600	0.574	0.554
0.300	0.672	0.652	0.632	0.615	0.594	0.569	0.550
0.400	0.664	0.644	0.625	0.608	0.588	0.564	0.545
0.500	0.654	0.635	0.616	0.600	0.581	0.558	0.540
0.600	0.643	0.624	0.606	0.590	0.572	0.551	0.534
0.700	0.628	0.610	0.593	0.579	0.562	0.543	0.527
0.800	0.609	0.593	0.577	0.564	0.549	0.532	0.516
0.900	0.580	0.566	0.553	0.543	0.531	0.513	0.482
0.950	0.555	0.544	0.534	0.524	0.510	0.474	0.402
0.980	0.530	0.519	0.507	0.491	0.461	0.401	0.343
0.990	0.517	0.505	0.489	0.469	0.435	0.381	0.333
1.000	0.501	0.486	0.467	0.445	0.412	0.360	0.322
1.010	0.485	0.468	0.446	0.425	0.392	0.350	0.309
1.020	0.467	0.448	0.428	0.403	0.376	0.345	-----
1.030	0.451	0.430	0.412	0.383	0.359	0.354	-----
1.040	0.451	0.368	0.439	0.339	-----	-----	-----

Table 4. Parameters that define the shape of the Bragg peak. Results pertain to an incident proton beam with a Gaussian energy spectrum, with a mean energy $\langle T_0 \rangle$ and with a standard deviation equal to P percent of the mean energy. The quantity r_0 is the CSDA at the mean energy.

z_m = depth at which depth-dose curve peaks
 D_m = peak value of depth-dose curve
 D_{rg} = dose at a depth $z = r_0$
 D_0 = entrance dose, at depth $z = 0$
 w_{80} = width of depth-dose curve at 80-percent level
 z_{80} = depth beyond Bragg peak where dose is 80 percent of peak
 w_{50} = width of depth-dose curve at 50-percent level
 z_{50} = depth beyond Bragg peak where dose is 50 percent of peak
 r_x = extrapolated range

Units: D_m , D_{rg} and D_0 are given in units of MeV cm²/g;
 z_m , w_{80} , z_{80} , w_{50} , z_{50} and r_x are given in units of the CSDA range r_0 .

$\langle T_0 \rangle = 240$ MeV, $r_0 = 35.41$ cm²/g

P	z_m	D_m	D_{rg}/D_m	D_0/D_m	w_{80}	z_{80}	w_{50}	z_{50}	r_x
0.0	0.9903	18.75	0.7936	3.3527	0.0231	0.9998	0.0680	1.0071	1.0161
0.5	0.9876	16.80	0.7894	3.0046	0.0299	0.9997	0.0889	1.0079	1.0208
1.0	0.9814	14.20	0.7874	2.5389	0.0444	0.9994	0.1417	1.0116	1.0311
1.5	0.9741	12.38	0.7861	2.2144	0.0620	0.9991	0.2191	1.0161	1.0431
2.0	0.9663	11.14	0.7839	1.9912	0.0812	0.9987	1.0164	1.0206	1.0557

$\langle T_0 \rangle = 200$ MeV, $r_0 = 25.96$ cm²/g

P	z_m	D_m	D_{rg}/D_m	D_0/D_m	w_{80}	z_{80}	w_{50}	z_{50}	r_x
0.0	0.9903	23.32	0.7991	4.0204	0.0236	1.0000	0.0674	1.0070	1.0164
0.5	0.9875	20.93	0.7926	3.6092	0.0302	0.9998	0.0871	1.0081	1.0212
1.0	0.9813	17.67	0.7906	3.0474	0.0446	0.9995	0.1350	1.0119	1.0317
1.5	0.9741	15.39	0.7898	2.6538	0.0620	0.9993	0.1994	1.0165	1.0439
2.0	0.9664	13.82	0.7882	2.3821	0.0808	0.9990	0.2803	1.0212	1.0567

$\langle T_0 \rangle = 160$ MeV, $r_0 = 17.65$ cm²/g

P	z_m	D_m	D_{rg}/D_m	D_0/D_m	w_{80}	z_{80}	w_{50}	z_{50}	r_x
0.0	0.9902	29.71	0.8018	4.7577	0.0239	1.0000	0.0669	1.0068	1.0167
0.5	0.9874	26.70	0.7952	4.2750	0.0305	0.9999	0.0859	1.0083	1.0217
1.0	0.9813	22.55	0.7935	3.6104	0.0448	0.9997	0.1301	1.0122	1.0322
1.5	0.9741	19.62	0.7929	3.1413	0.0620	0.9995	0.1865	1.0169	1.0446
2.0	0.9665	17.59	0.7919	2.8159	0.0804	0.9993	0.2519	1.0218	1.0576

Table 4, continued.

$$\langle T_o \rangle = 130 \text{ MeV}, r_o = 12.28 \text{ cm}^2/\text{g}$$

P	z_m	D_m	D_{rg}/D_m	D_o/D_m	w_{80}	z_{80}	w_{50}	z_{50}	r_x
0.0	0.9901	36.55	0.8019	5.3257	0.0242	1.0001	0.0669	1.0069	1.0173
0.5	0.9873	32.82	0.7978	4.7817	0.0309	0.9999	0.0858	1.0085	1.0222
1.0	0.9812	27.72	0.7960	4.0384	0.0453	0.9998	0.1283	1.0125	1.0328
1.5	0.9740	24.10	0.7958	3.5113	0.0625	0.9997	0.1812	1.0173	1.0454
2.0	0.9664	21.59	0.7952	3.1445	0.0808	0.9996	0.2403	1.0223	1.0586

$$\langle T_o \rangle = 100 \text{ MeV}, r_o = 7.718 \text{ cm}^2/\text{g}$$

P	z_m	D_m	D_{rg}/D_m	D_o/D_m	w_{80}	z_{80}	w_{50}	z_{50}	r_x
0.0	0.9900	46.53	0.8105	5.8537	0.0249	1.0003	0.0679	1.0072	1.0180
0.5	0.9872	41.89	0.8044	5.2702	0.0315	1.0001	0.0862	1.0089	1.0228
1.0	0.9811	35.44	0.8008	4.4585	0.0458	1.0000	0.1271	1.0130	1.0335
1.5	0.9740	24.10	0.7958	3.5113	0.0625	0.9997	0.1812	1.0173	1.0454
2.0	0.9664	27.59	0.7991	3.4697	0.0811	0.9999	0.2318	1.0229	1.0596

$$\langle T_o \rangle = 70 \text{ MeV}, r_o = 4.0801 \text{ cm}^2/\text{g}$$

P	z_m	D_m	D_{rg}/D_m	D_o/D_m	w_{80}	z_{80}	w_{50}	z_{50}	r_x
0.0	0.9902	63.34	0.8202	6.3025	0.0257	1.0006	0.0697	1.0078	1.0189
0.5	0.9873	57.25	0.8154	5.6961	0.0321	1.0005	0.0875	1.0095	1.0238
1.0	0.9812	48.60	0.8090	4.8350	0.0465	1.0005	0.1270	1.0136	1.0345
1.5	0.9741	42.30	0.8062	4.2087	0.0635	1.0004	0.1749	1.0185	1.0473
2.0	0.9666	37.87	0.8045	3.7674	0.0815	1.0004	0.2264	1.0236	1.0608

$$\langle T_o \rangle = 50 \text{ MeV}, r_o = 2.227 \text{ cm}^2/\text{g}$$

P	z_m	D_m	D_{rg}/D_m	D_o/D_m	w_{80}	z_{80}	w_{50}	z_{50}	r_x
0.0	0.9903	83.50	0.8462	6.7103	0.0268	1.0016	0.0719	1.0087	1.0196
0.5	0.9877	75.74	0.8360	6.0868	0.0324	1.0014	0.0893	1.0105	1.0251
1.0	0.9817	64.63	0.8229	5.1940	0.0471	1.0012	0.1273	1.0145	1.0357
1.5	0.9746	56.38	0.8164	4.5309	0.0639	1.0011	0.1730	1.0193	1.0484
2.0	0.9671	50.51	0.8127	4.0590	0.0818	1.0011	0.2216	1.0245	1.0619

Table 5. Comparison with experimental depth-dose curve of Gottschalk (1992). The theoretical curve was calculated assuming a Gaussian beam spectrum with a mean energy $\langle T_0 \rangle = 158.5$ MeV and a standard deviation equal to 0.95% of $\langle T_0 \rangle$. Depths are expressed in units of the CSDA range $r_0 = 17.36$ g/cm² at 158.5 MeV.

z/r_0	Exp.	Calc.	% Diff.
0.165	0.27440	0.27526	-0.3
0.396	0.30217	0.28998	4.2
0.626	0.34211	0.32662	4.7
0.799	0.41194	0.40004	3.0
0.920	0.58441	0.58069	0.6
0.954	0.77237	0.77928	-0.9
0.977	0.99052	0.98866	0.2
0.995	0.84401	0.89849	-6.1
1.006	0.43931	0.64708	-32.1
1.018	0.12276	0.35846	-65.8
1.029	0.01892	0.14928	-87.3
1.041	0.00553	0.04617	-88.0
1.052	0.00272	0.01052	-74.2

Table 6. Comparison with experimental relative depth-dose of Larsson (1961). The theoretical curve was calculated assuming a Gaussian beam spectrum with a mean energy $\langle T_0 \rangle = 188.4$ MeV and a standard deviation equal to 0.5% of $\langle T_0 \rangle$. Depths are expressed in units of the CSDA range $r_0 = 23.43$ g/cm² at 188.4 MeV.

z/r_0	Exp.	Calc.	% Diff.
0.122	0.239	0.263	-9.0
0.255	0.252	0.264	-4.6
0.301	0.256	0.265	-3.5
0.447	0.268	0.272	-1.5
0.487	0.274	0.276	-0.7
0.531	0.279	0.280	-0.4
0.577	0.285	0.286	-0.3
0.616	0.292	0.292	-0.3
0.659	0.302	0.301	0.3
0.703	0.316	0.312	1.2
0.745	0.333	0.326	1.9
0.788	0.350	0.346	1.2
0.831	0.377	0.373	0.9
0.872	0.414	0.413	0.3
0.892	0.437	0.441	-0.8
0.914	0.465	0.483	-3.6
0.925	0.502	0.510	-1.6
0.935	0.545	0.543	0.4
0.944	0.577	0.581	-0.6
0.948	0.620	0.605	2.6
0.954	0.655	0.641	2.2
0.963	0.741	0.717	3.3
0.969	0.798	0.791	1.0
0.974	0.854	0.860	-0.7
0.977	0.885	0.913	-3.1
0.978	0.925	0.929	-0.4
0.981	0.949	0.960	-1.1
0.982	0.972	0.969	0.3
0.986	0.989	0.996	-0.7
0.988	1.000	1.000	0.0
0.994	0.990	0.951	4.1
0.995	0.939	0.929	1.2
0.997	0.860	0.873	-1.5
1.000	0.728	0.789	-7.7
1.002	0.665	0.735	-9.5
1.004	0.447	0.663	-32.7
1.006	0.370	0.572	-35.3
1.008	0.284	0.496	-42.7
1.012	0.220	0.349	-37.1
1.015	0.147	0.262	-44.0
1.024	0.043	0.086	-49.4

Table 7. Comparison with experimental depth-dose curve of Scheib and Pedroni (1992). The theoretical curve was calculated assuming a Gaussian beam spectrum with a mean energy $\langle T_0 \rangle = 214.5$ MeV and a standard deviation equal to 0.4% of $\langle T_0 \rangle$. Depths are expressed in units of the CSDA range $r_0 = 29.26$ g/cm² at 212.5 MeV.

z/r_0	Exp.	Calc.	% Diff.
0.220	0.270	0.279	-3.3
0.255	0.268	0.279	-4.0
0.289	0.268	0.278	-3.6
0.323	0.270	0.278	-3.2
0.357	0.275	0.279	-1.2
0.391	0.278	0.279	-0.7
0.425	0.278	0.280	-0.7
0.460	0.282	0.282	0.2
0.494	0.284	0.284	0.2
0.528	0.291	0.286	1.6
0.562	0.293	0.289	1.3
0.596	0.299	0.293	2.1
0.630	0.305	0.298	2.4
0.665	0.315	0.304	3.8
0.699	0.319	0.311	2.6
0.733	0.334	0.321	4.1
0.767	0.346	0.333	3.9
0.801	0.364	0.349	4.3
0.836	0.382	0.370	3.1
0.870	0.416	0.401	3.8
0.904	0.462	0.449	2.9
0.938	0.549	0.536	2.4
0.945	0.572	0.564	1.4
0.952	0.607	0.600	1.1
0.959	0.650	0.647	0.3
0.965	0.713	0.713	0.0
0.972	0.800	0.803	-0.4
0.979	0.904	0.910	-0.7
0.986	0.988	0.991	-0.4
0.993	0.975	0.973	0.2
1.000	0.795	0.809	-1.7
1.006	0.509	0.542	-6.0
1.013	0.243	0.282	-14.0
1.020	0.085	0.112	-23.7
1.027	0.021	0.033	-37.7
1.034	0.003	0.007	-53.1
1.041	0.000	0.001	-100.0

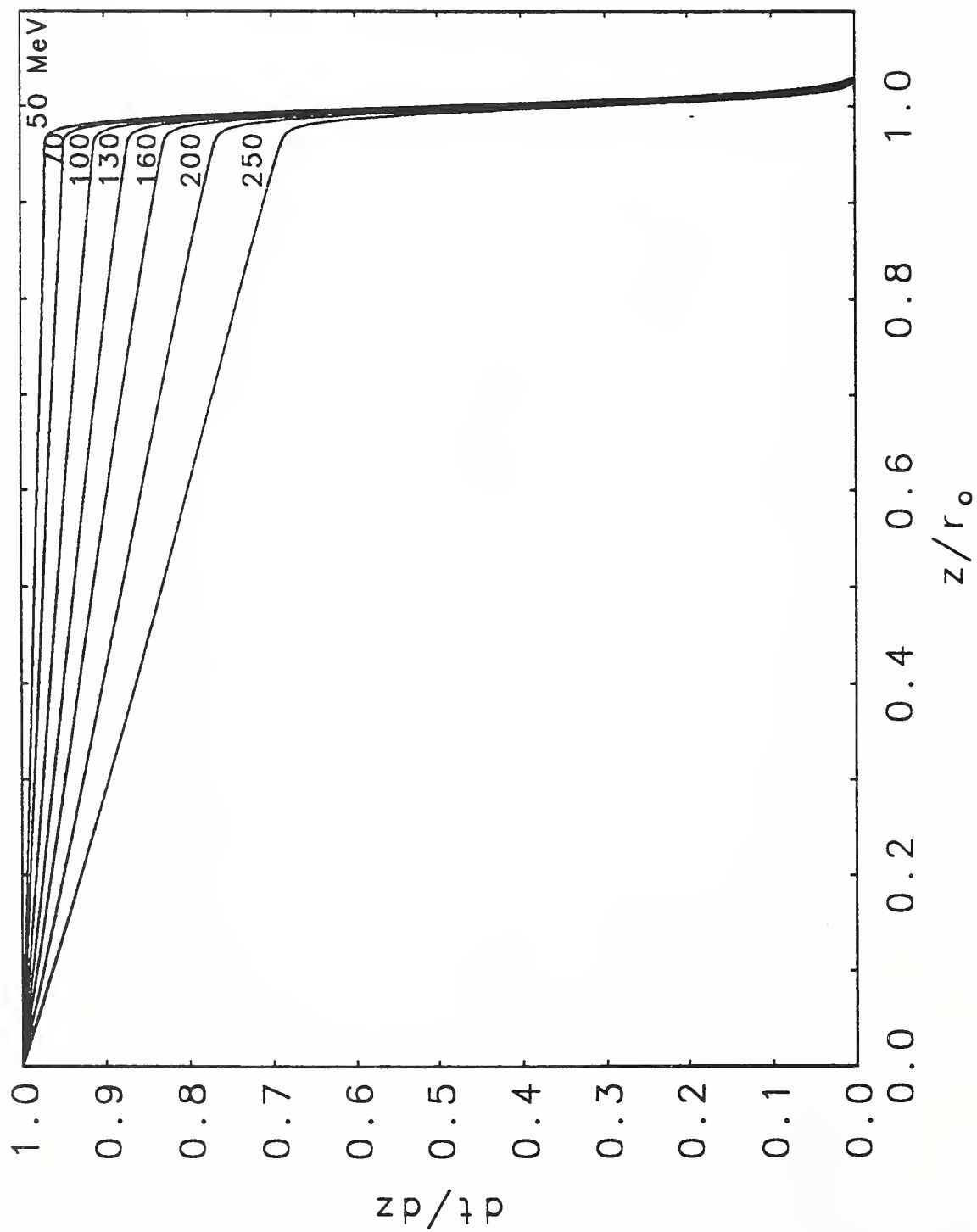


Fig. 1a. Average track length per unit depth of primary protons, for beams with energy $T_0 = 50, 70, 100, 130, 160, 200$ or 250 MeV. Track length distributions over entire range.

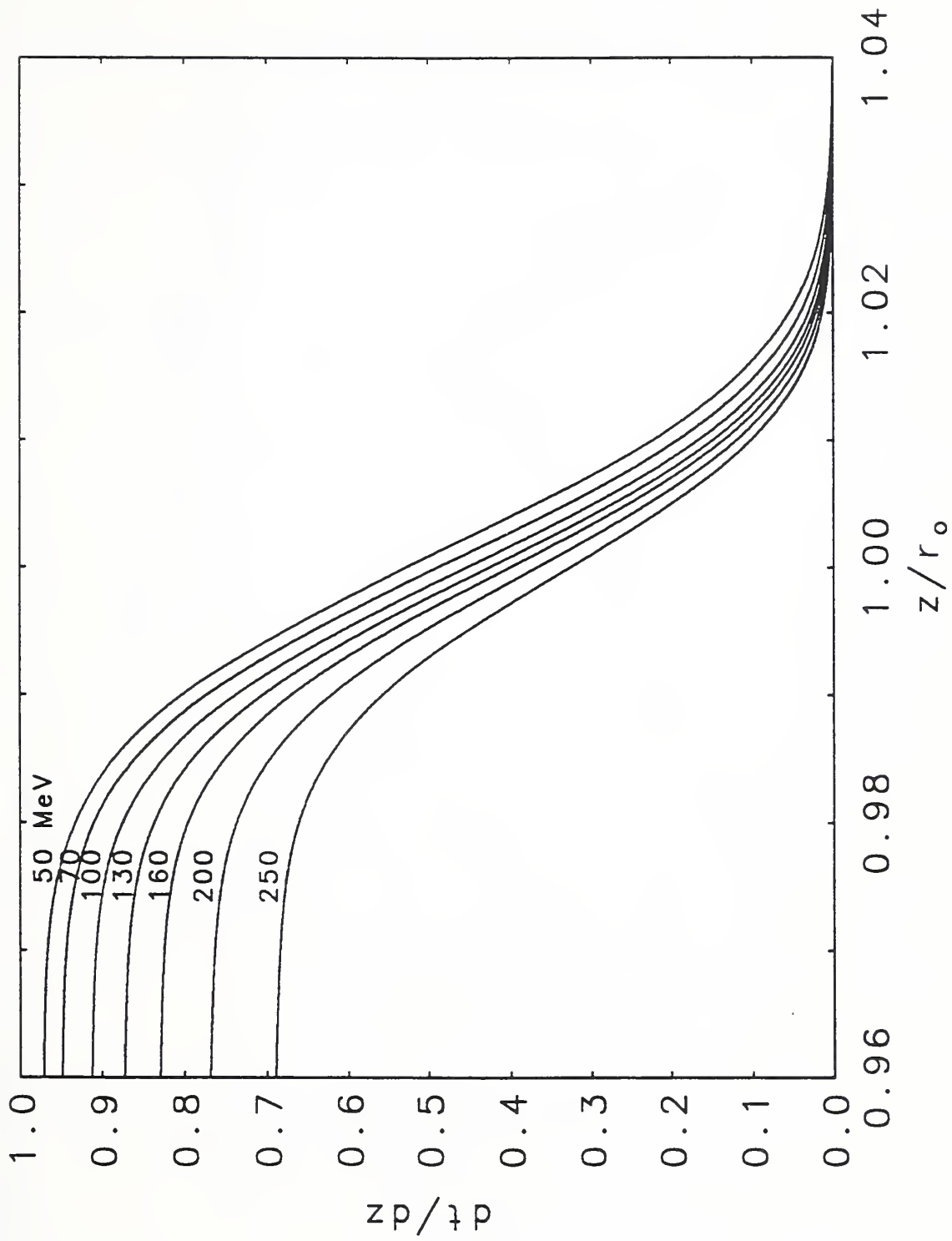


Fig. 1b. Average track length per unit depth of primary protons, for beams with energy $T_0 = 50, 70, 100, 130, 160, 200$ or 250 MeV. Track length distributions at great depth, near and beyond the Bragg peak.

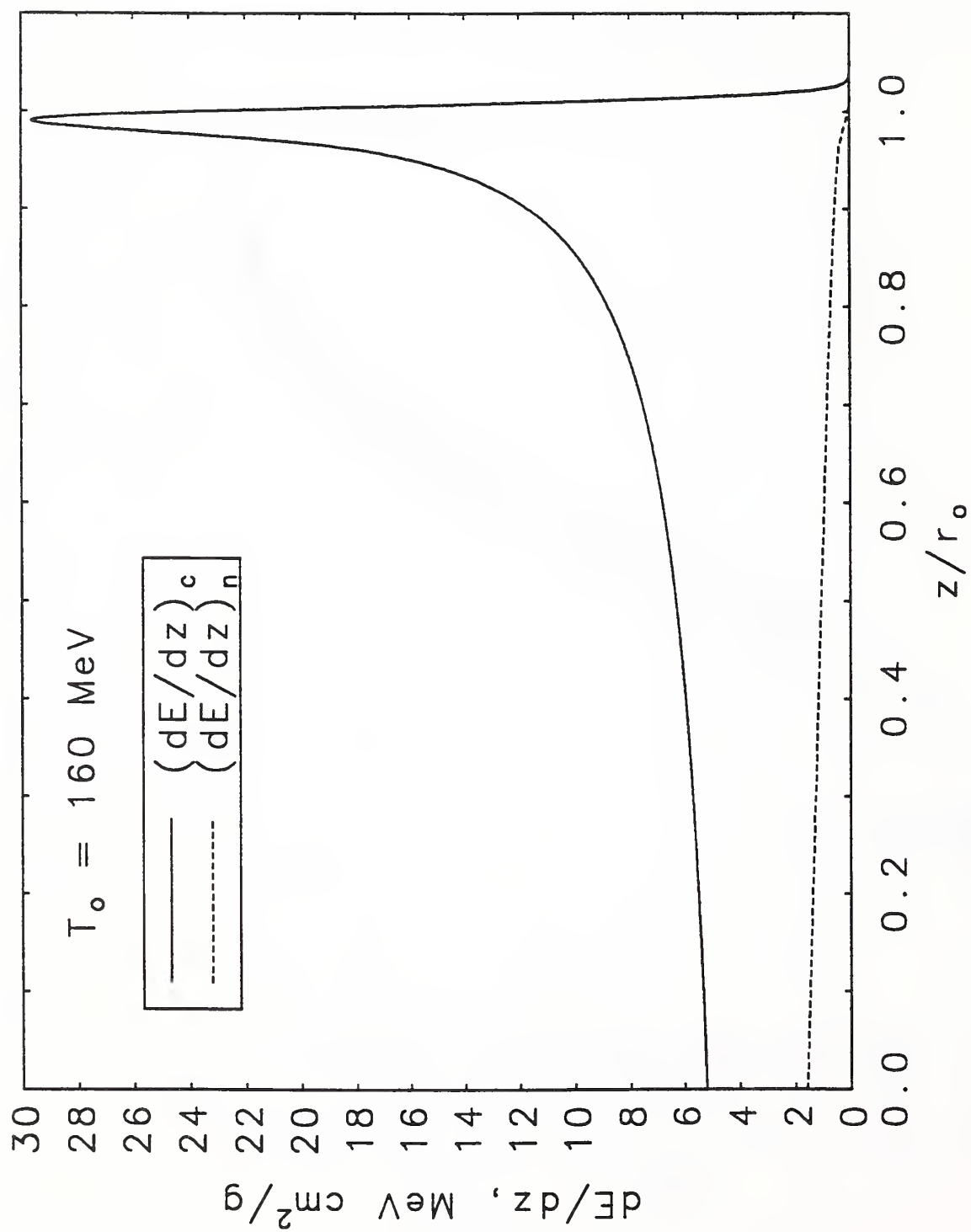


Fig. 2. Average energy loss per unit depth due to Coulomb interactions, $(dE/dz)_c$, and due nuclear reactions, $(dE/dz)_n$.

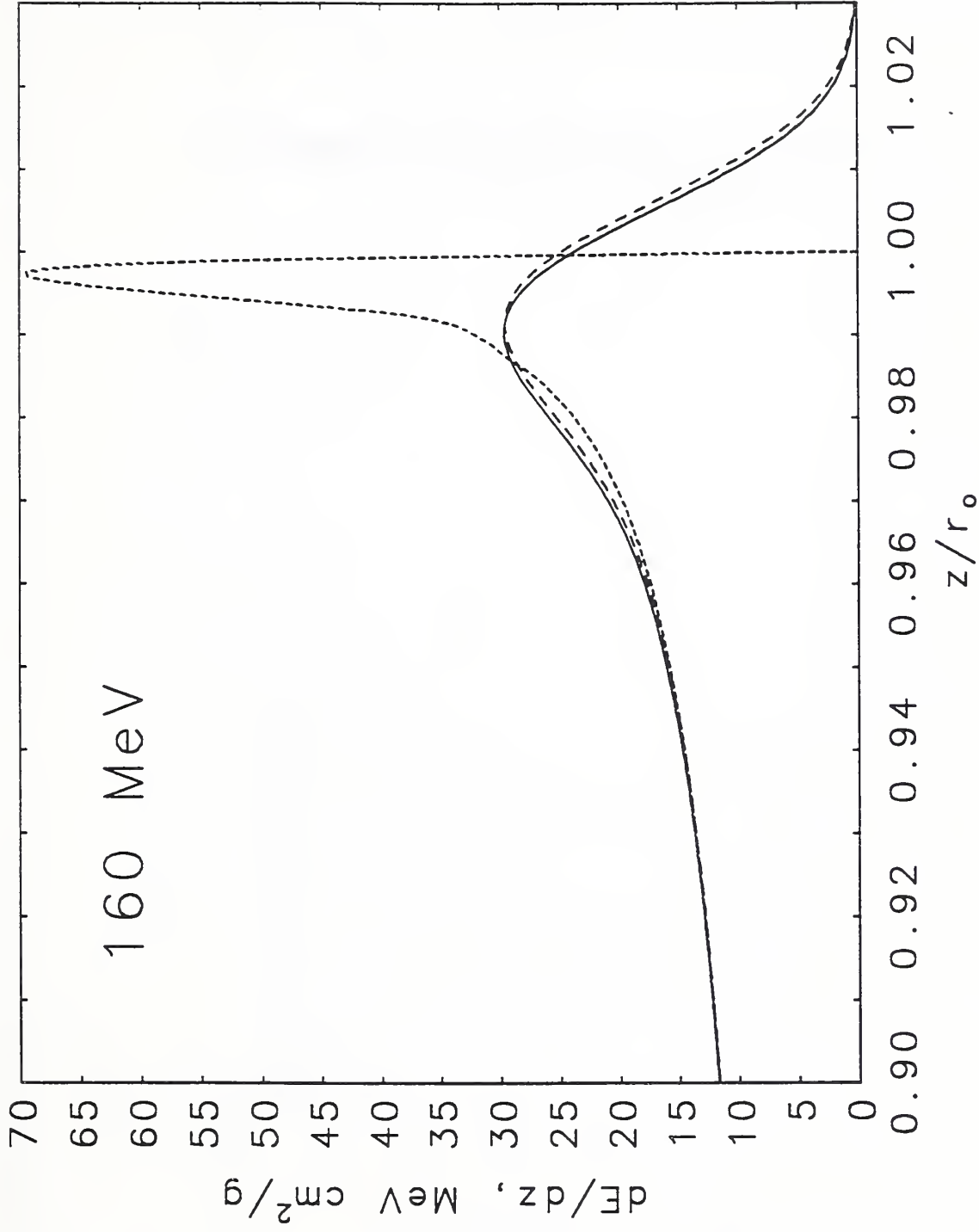


Fig. 3. Model study pertaining to the average energy loss of a proton beam per unit depth, due to Coulomb interactions. Solid curve: Complete treatment, with energy-loss straggling and multiple-scattering deflections. Dotted curve: With multiple-scattering deflections, and with energy-loss straggling disregarded. Dashed curve: With energy-loss straggling, and with multiple-scattering deflections disregarded.

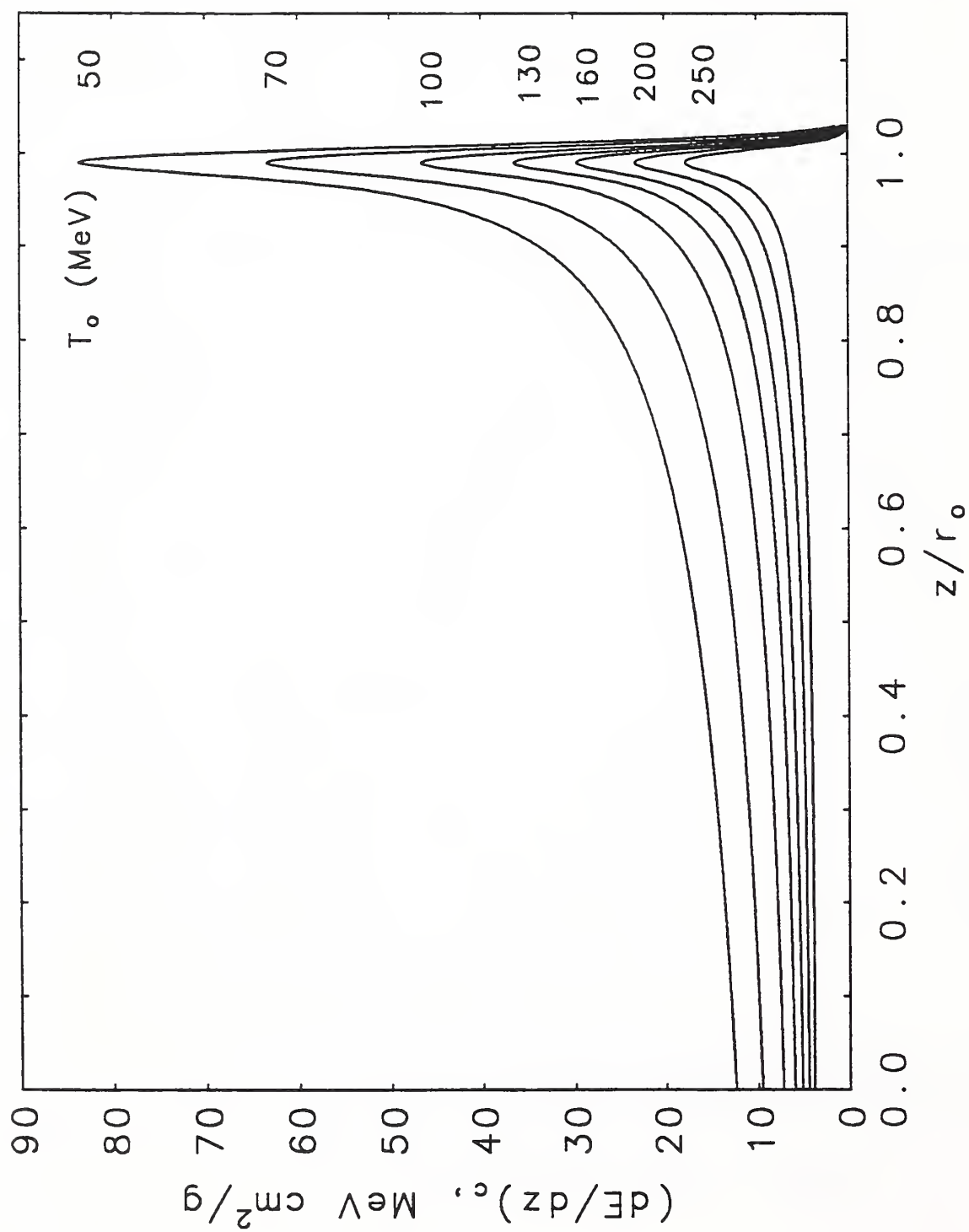


Fig. 4. Average energy loss per unit depth due to Coulomb interactions, for beams with energy $T_0 = 50, 70, 100, 130, 160, 200$ or 250 MeV.

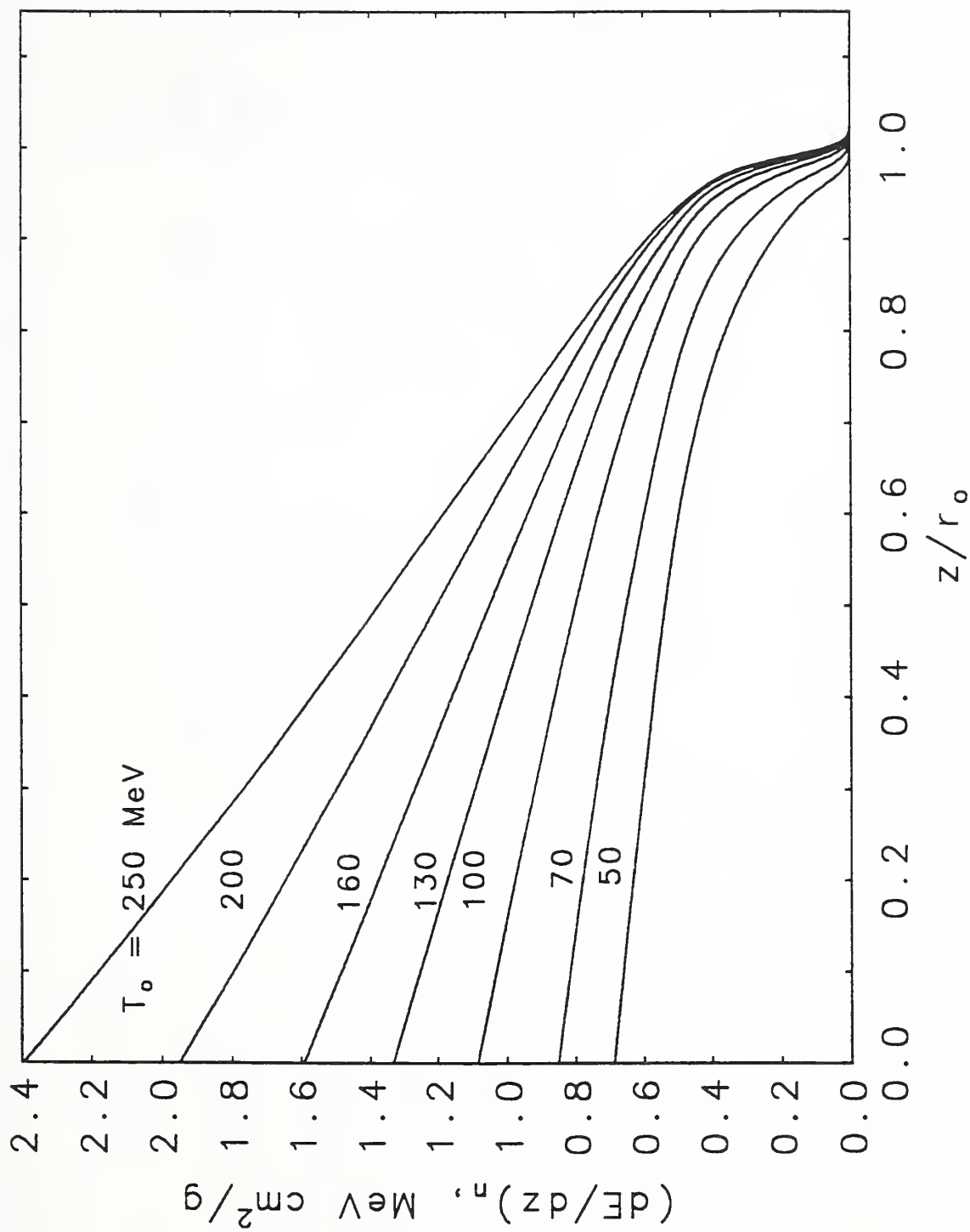


Fig. 5. Average energy loss per unit depth due to nuclear reactions, for beams with energy $T_0 = 50, 70, 100, 130, 160, 200$, or 250 MeV .

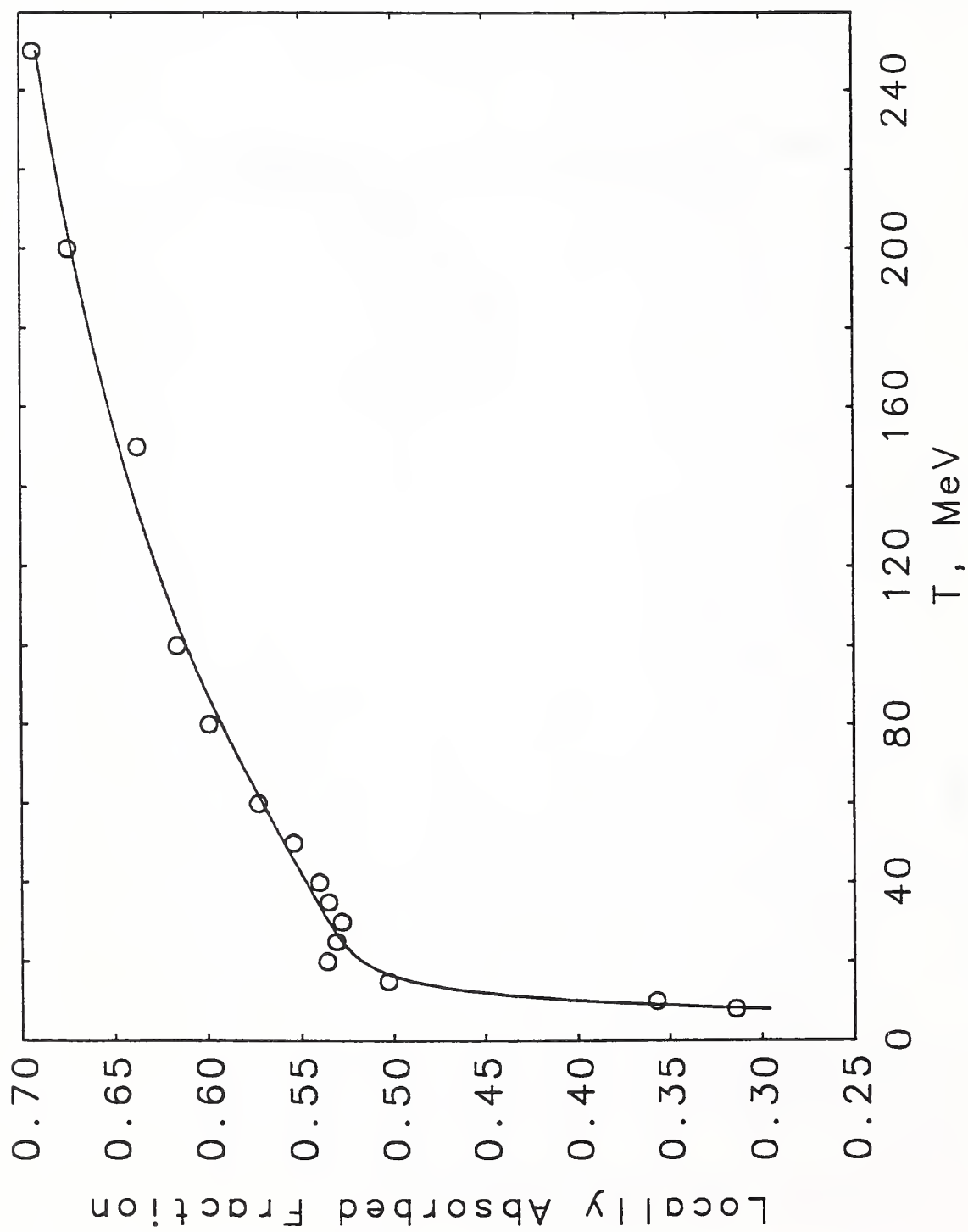


Fig. 6. Fraction of the energy lost by a proton in a nonelastic nuclear reaction that is transferred to secondary charged particles (Seltzer, 1992). The points represent the calculations, and the curve is a least-squares fit.

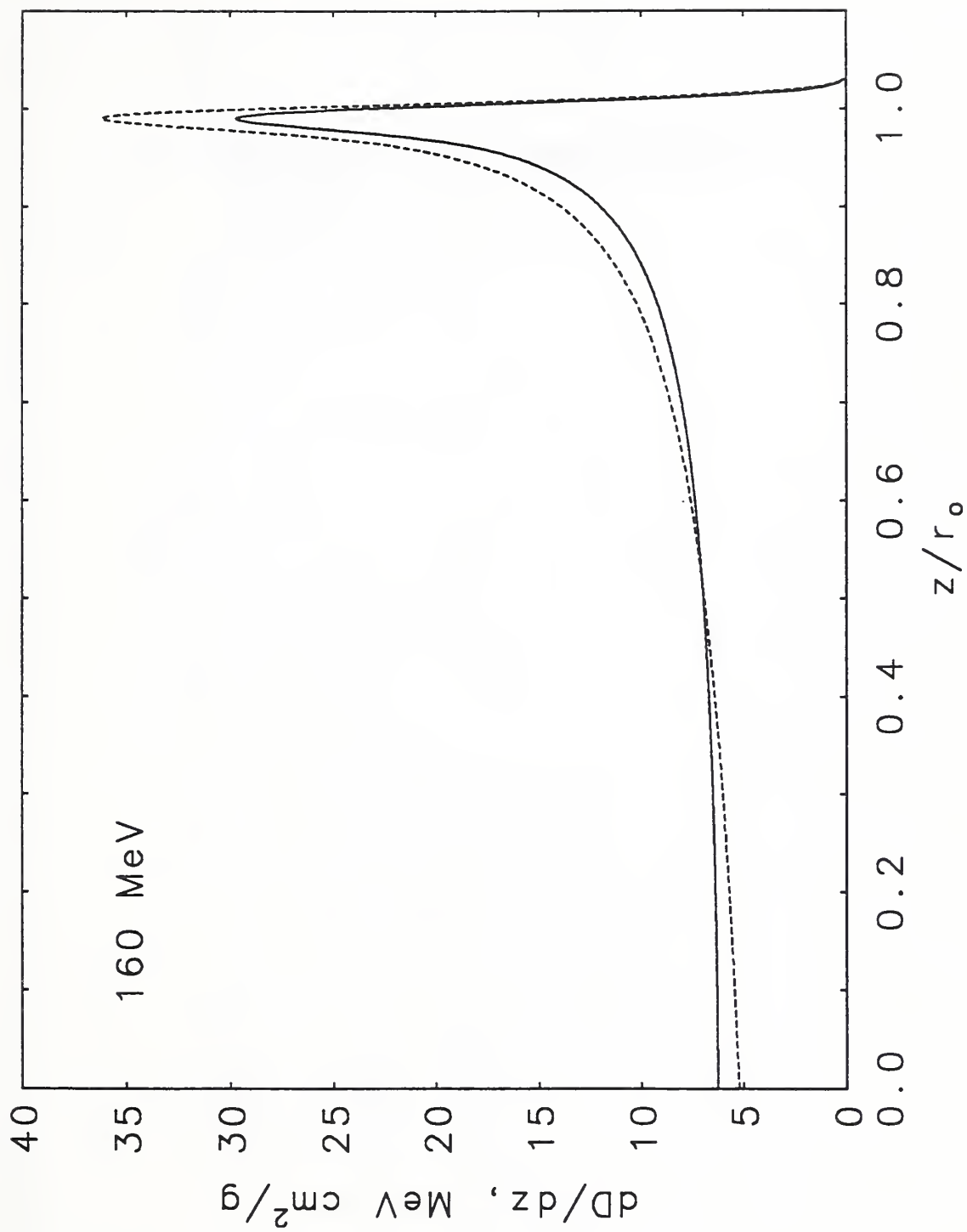


Fig. 7. Depth-dose distribution from 160-MeV proton beam. The solid curve takes into account nuclear reactions; the dotted curve disregards them.

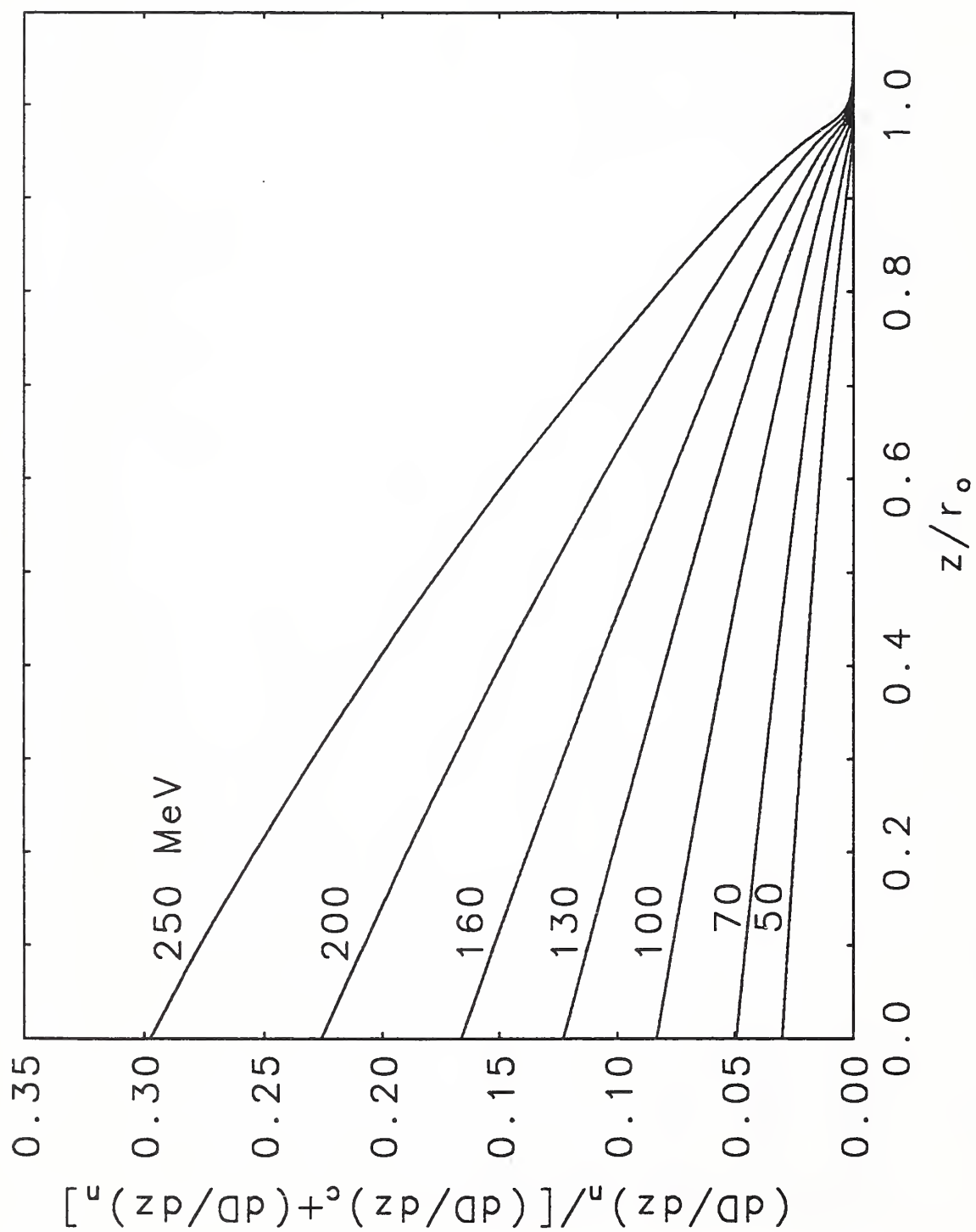


Fig. 8. Fraction of the absorbed dose that is contributed by secondary charged particles from nuclear reactions.

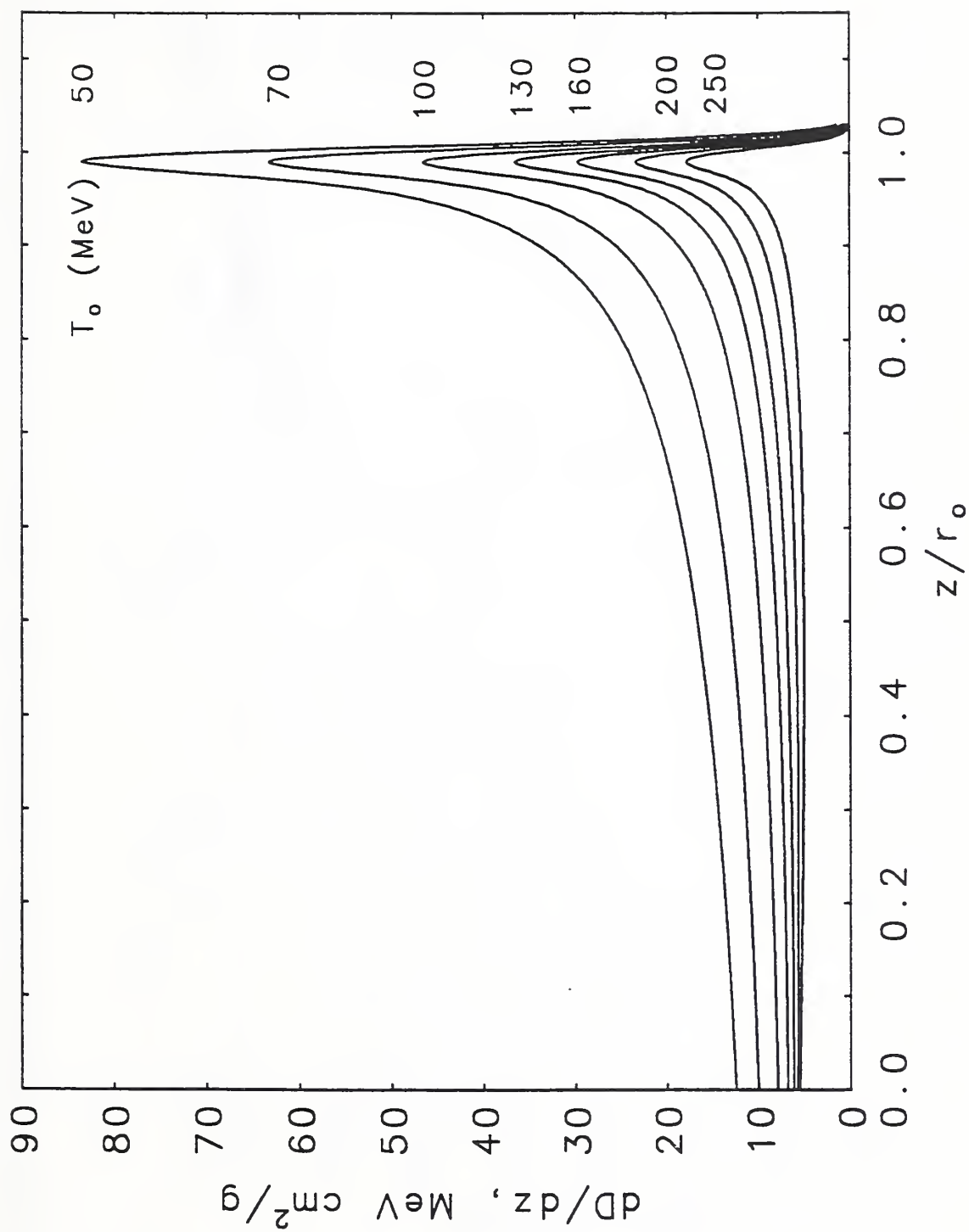


Fig. 9a. Average amount of energy deposited per unit depth. Results are for beams with energy $T_0 = 50, 70, 100, 130, 160, 200$ or 250 MeV. Complete depth-dose curves.

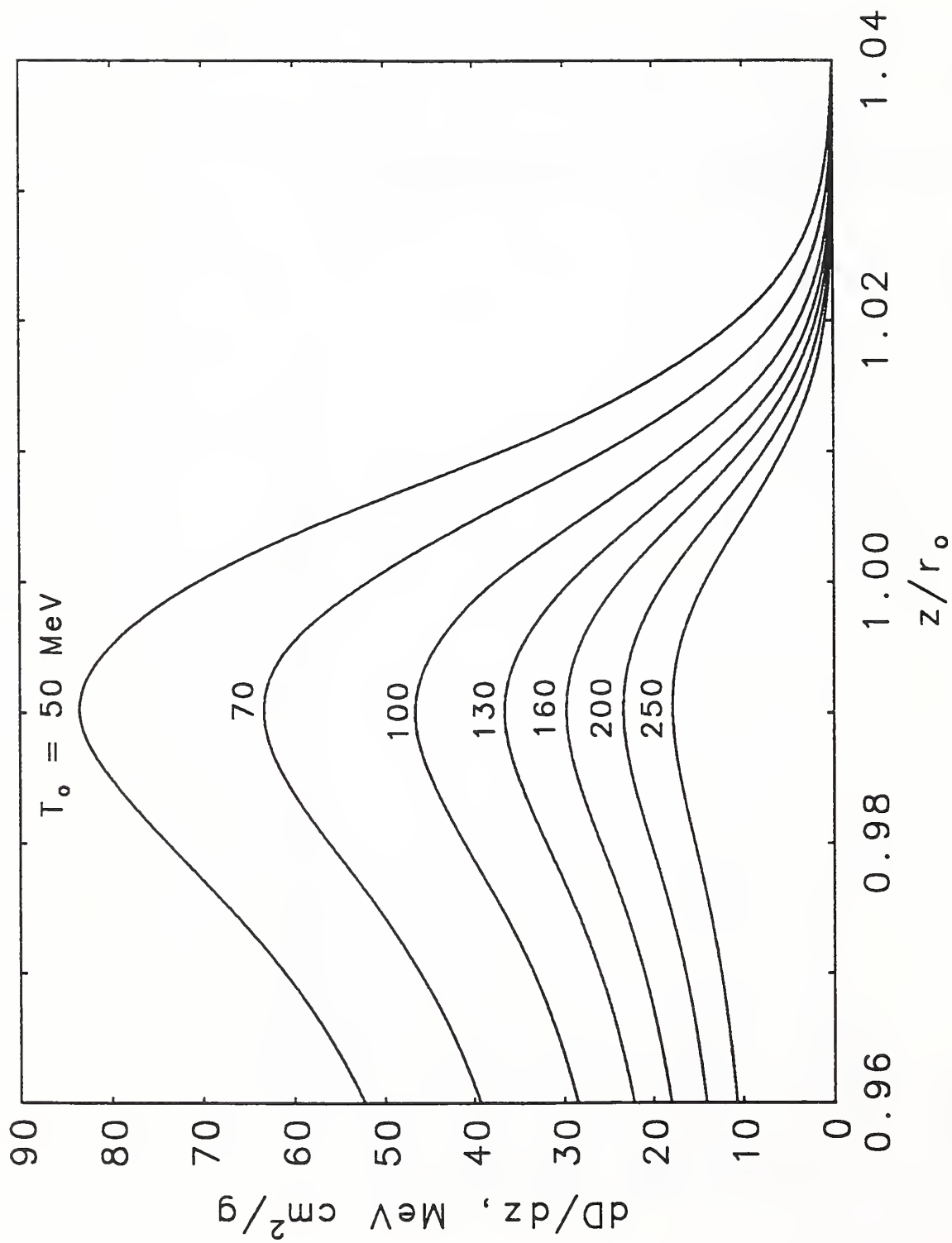


Fig. 9b. Average amount of energy deposited per unit depth. Results are for beams with energy $T_0 = 50, 70, 100, 130, 160, 200$ or 250 MeV. Depth-dose curves near and beyond the Bragg peak.

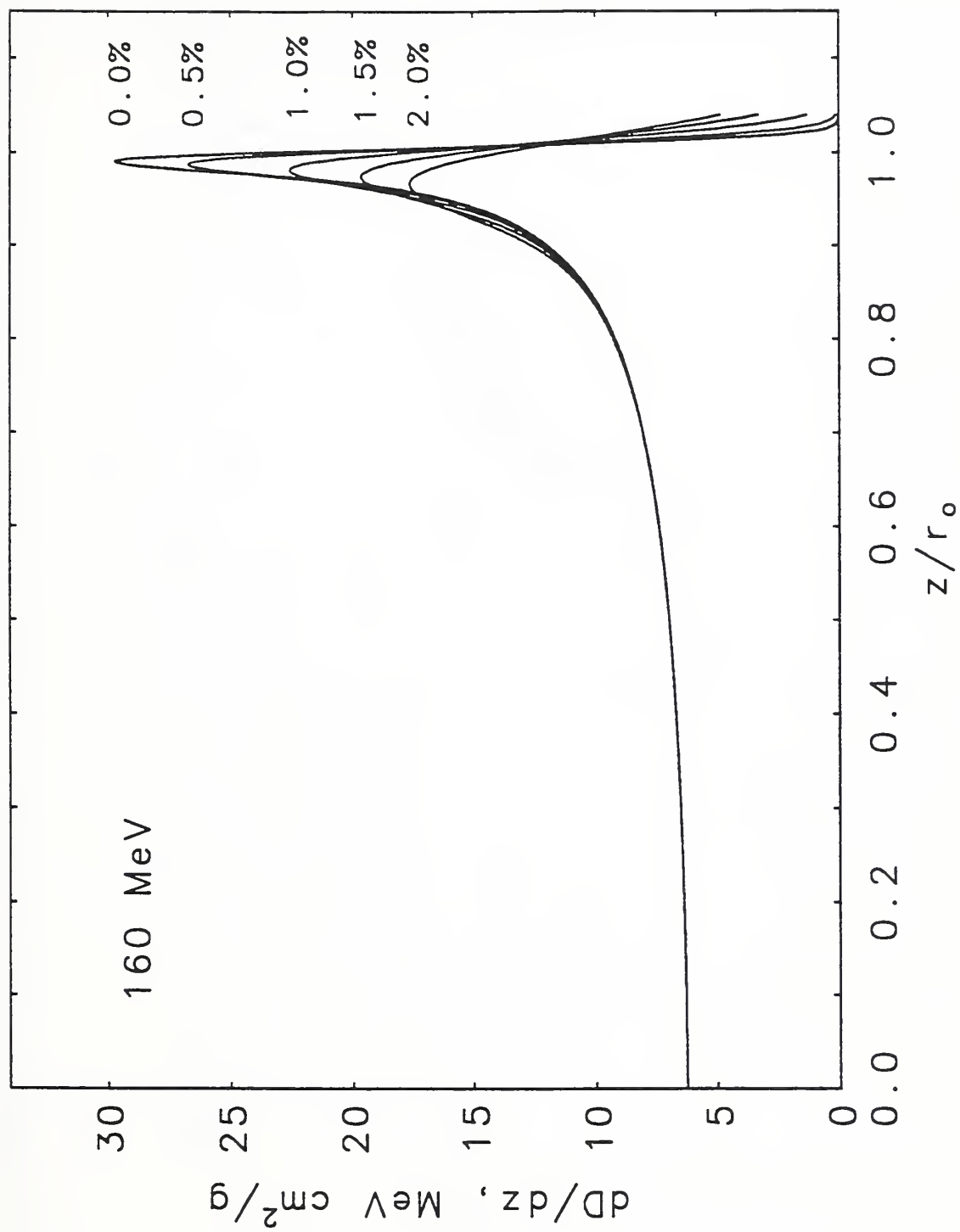


Fig. 10a. Average amount of energy deposited per unit depth. Results are for protons beams incident with a Gaussian energy spectrum. The mean energy of the spectrum is 160 MeV, and the standard deviation is equal to a percentage of the average energy, as indicated by the labels on the curves. Complete depth-dose curves.

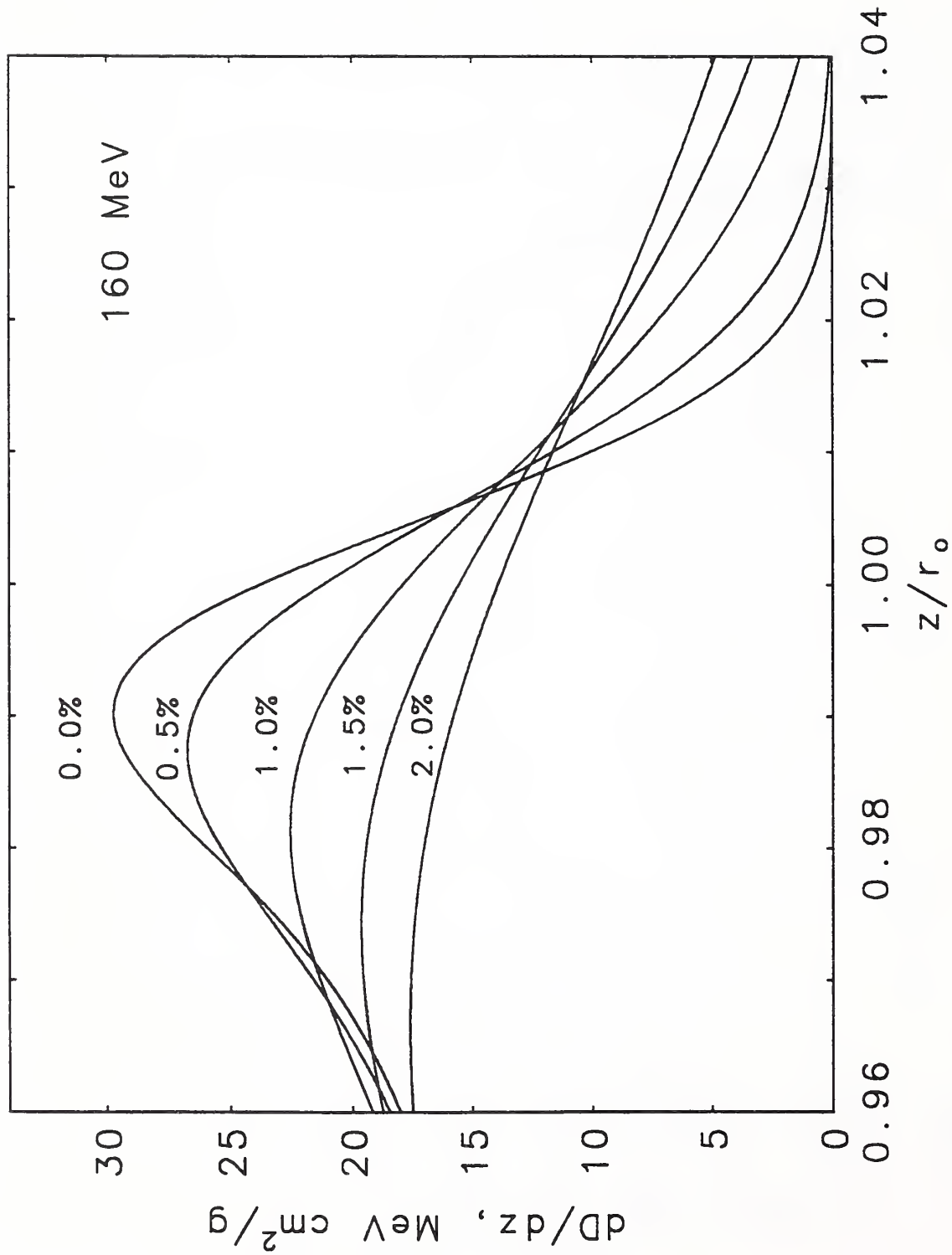


Fig. 10b. Average amount of energy deposited per unit depth. Results are for protons beams incident with a Gaussian energy spectrum. The mean energy of the spectrum is 160 MeV, and the standard deviation is equal to a percentage of the average energy, as indicated by the labels on the curves. Depth-dose curves near and beyond the Bragg peak.

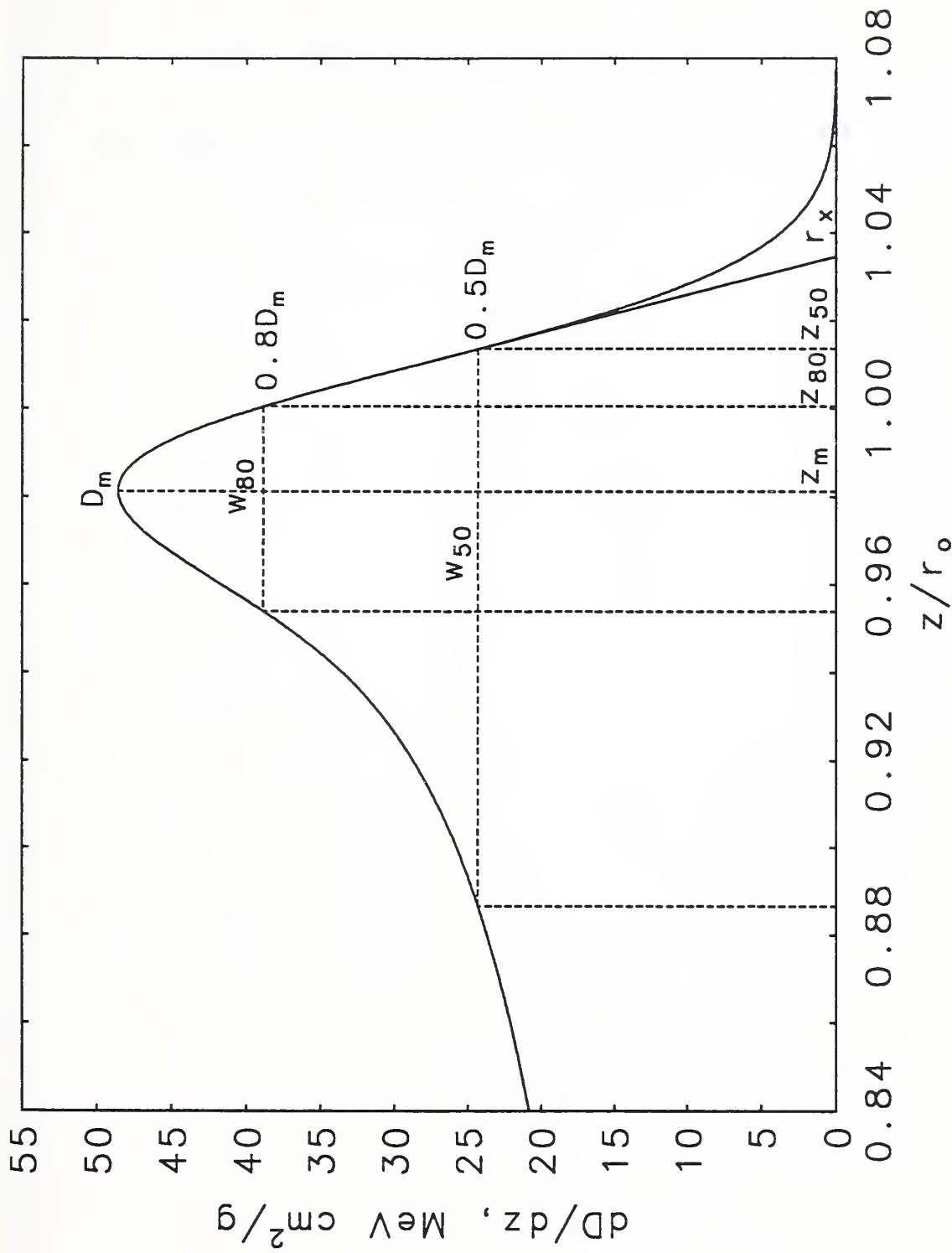


Fig. 11. Parameters that characterize the depth dose curve in the region of the Bragg peak. The quantities z_m , z_{80} , and z_{50} are the depths at which the depth-dose curve peaks, or is equal to 80%, respectively 50%, of the peak value D_m ; w_{80} and w_{50} are the widths of the Bragg peak at the 80%, respectively, 50% level. The quantity r_x is the extrapolated range. The numerical values of the parameters pertain to a 70-MeV proton beam.

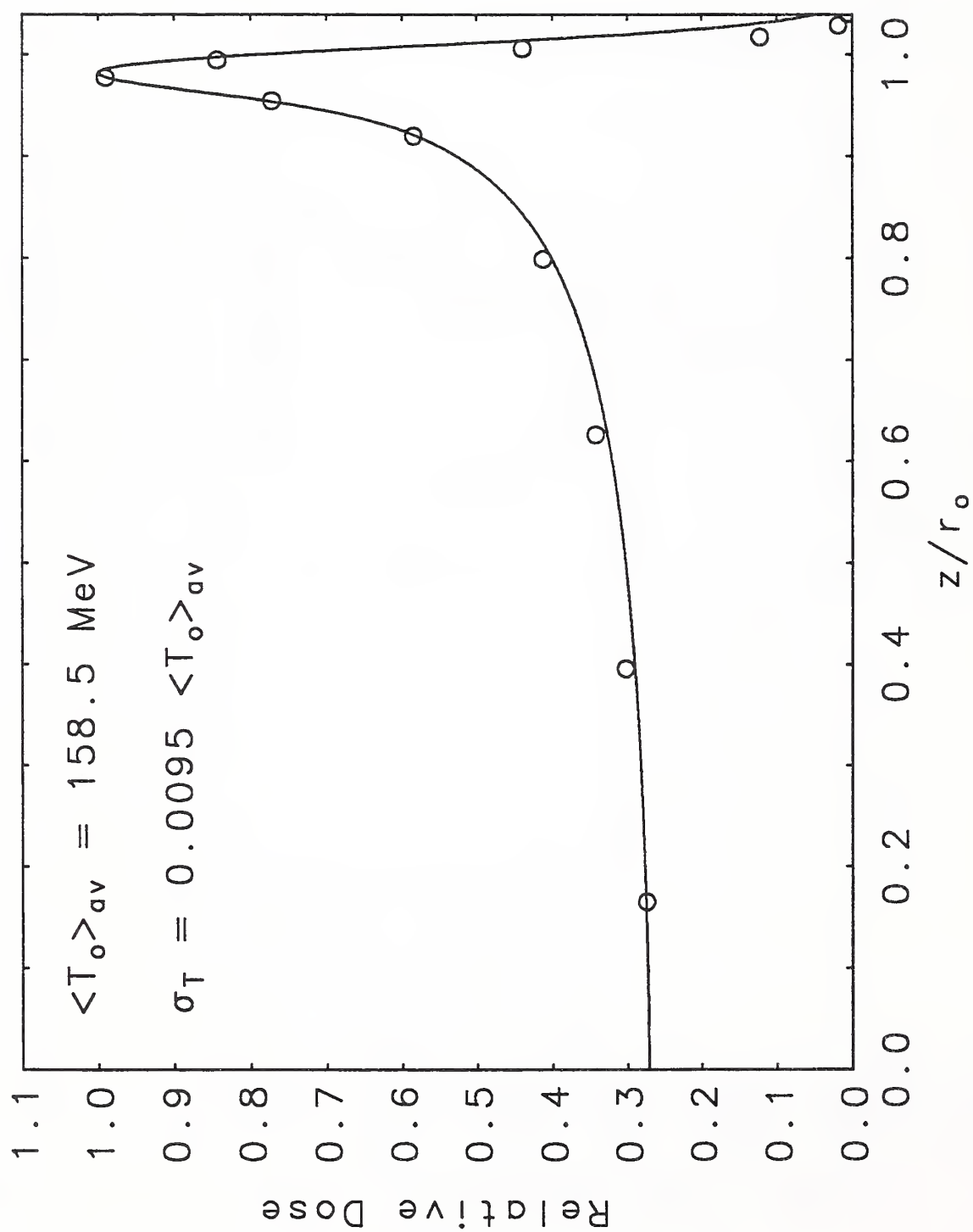


Fig. 12. Comparison of calculated and measured depth-dose distributions. The curve is calculated, and the points (o) are from an experiment at the Harvard Cyclotron Laboratory (Gottschalk, 1992).

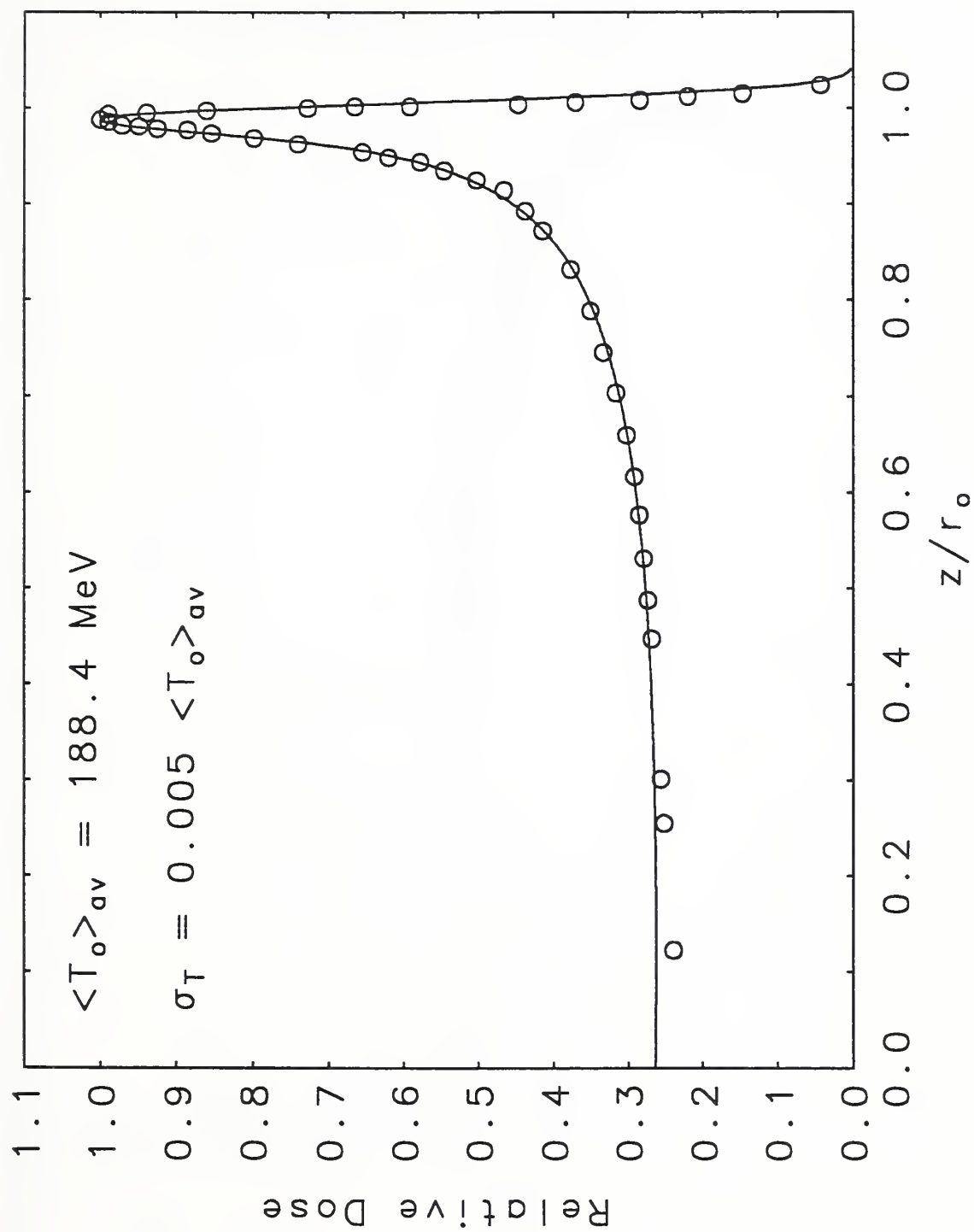


Fig. 13. Comparison of calculated and measured depth-dose distributions. The curve is calculated, and the points (o) are from an experiment by Larsson (1961).

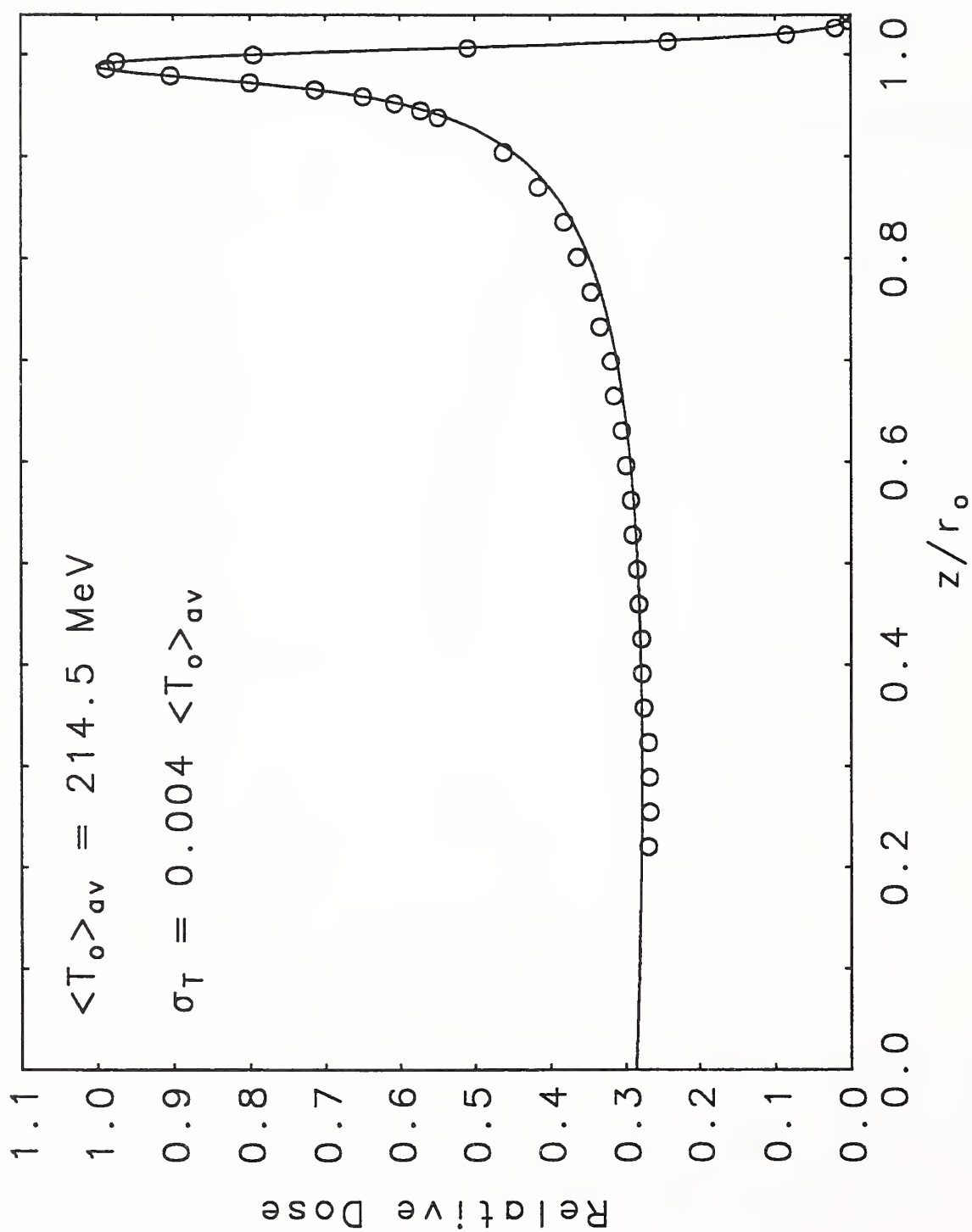


Fig. 14. Comparison of calculated and measured depth-dose distributions. The curve is calculated, and the points (o) are from an experiment at the Paul Scherrer Institute (Scheib and Pedroni, 1992).

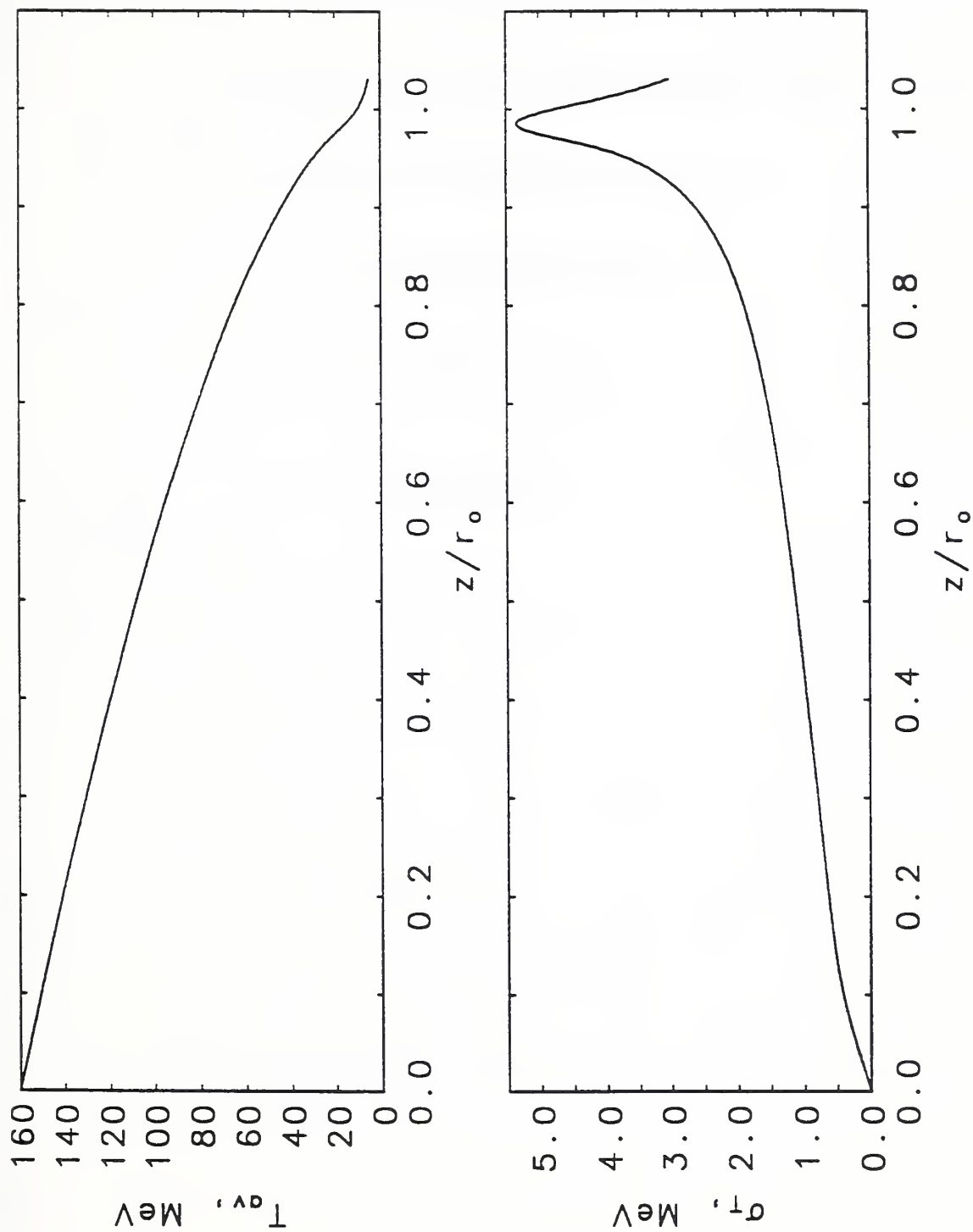


Fig. 15. Average energy T_{av} and standard deviation σ_T of the proton spectrum, as function of depth, for a beam incident with an energy of 160 MeV. T_{av} and σ_T were obtained by averaging over the track length distribution $y(T, z)$.

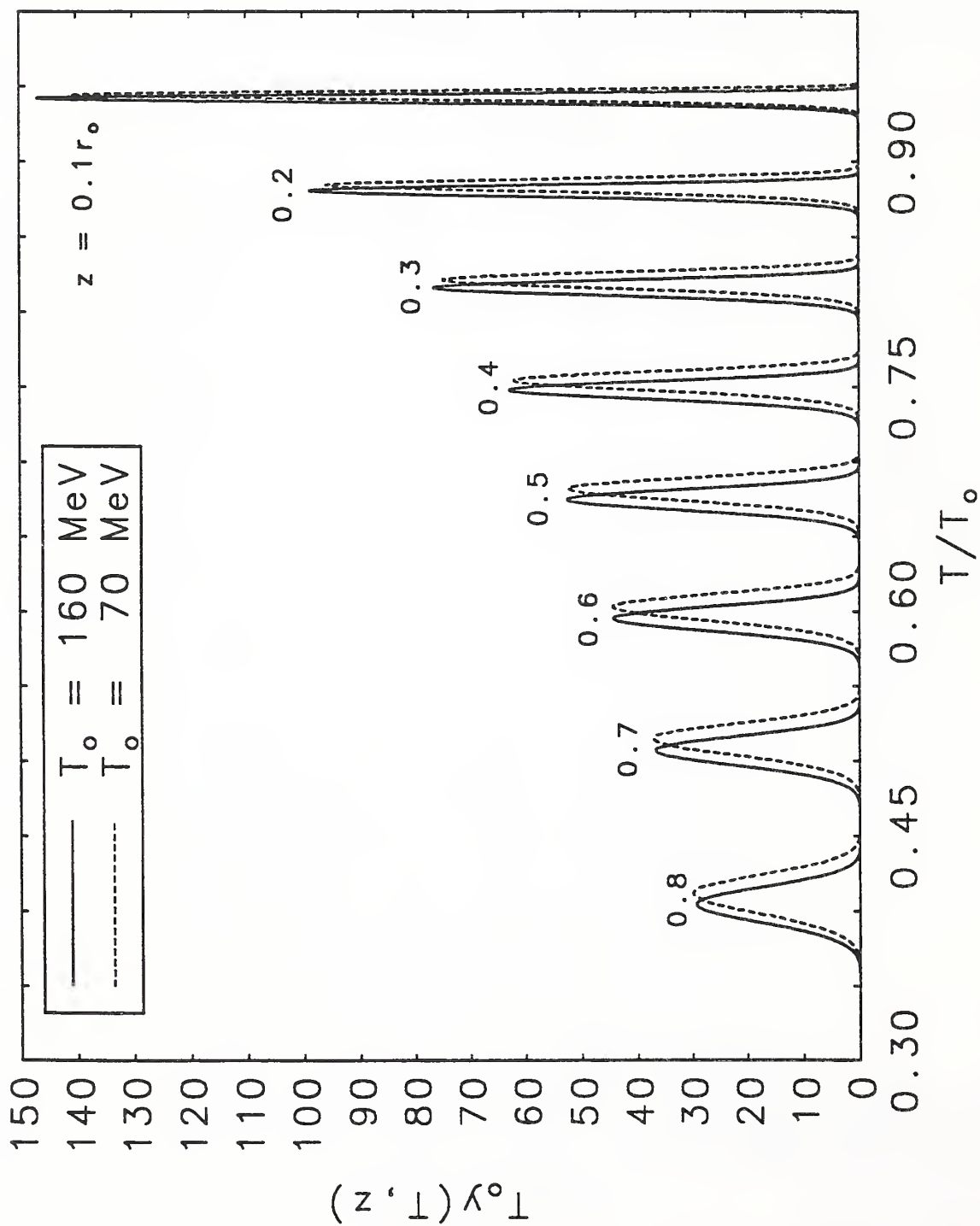


Fig. 16a. Scaled proton energy spectra for proton beams incident beams with energy $T_0 = 160$ and 70 MeV . Spectra at depths from 10% to 80% of r_0 .

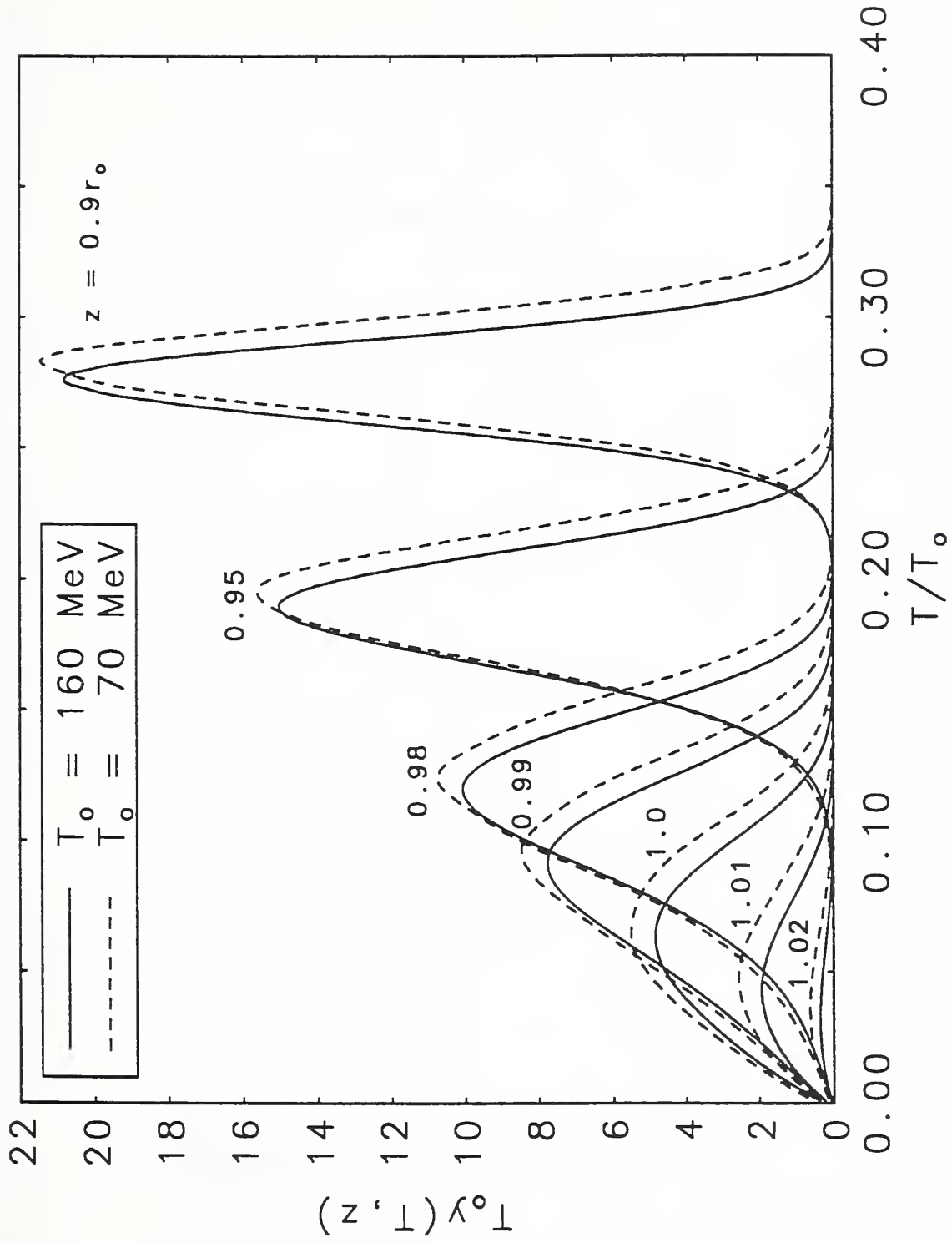


Fig. 16b. Scaled proton energy spectra for proton beams incident beams with energy $T_0 = 160$ and 70 MeV. Spectra at depths from 90% to 102% of r_0 .

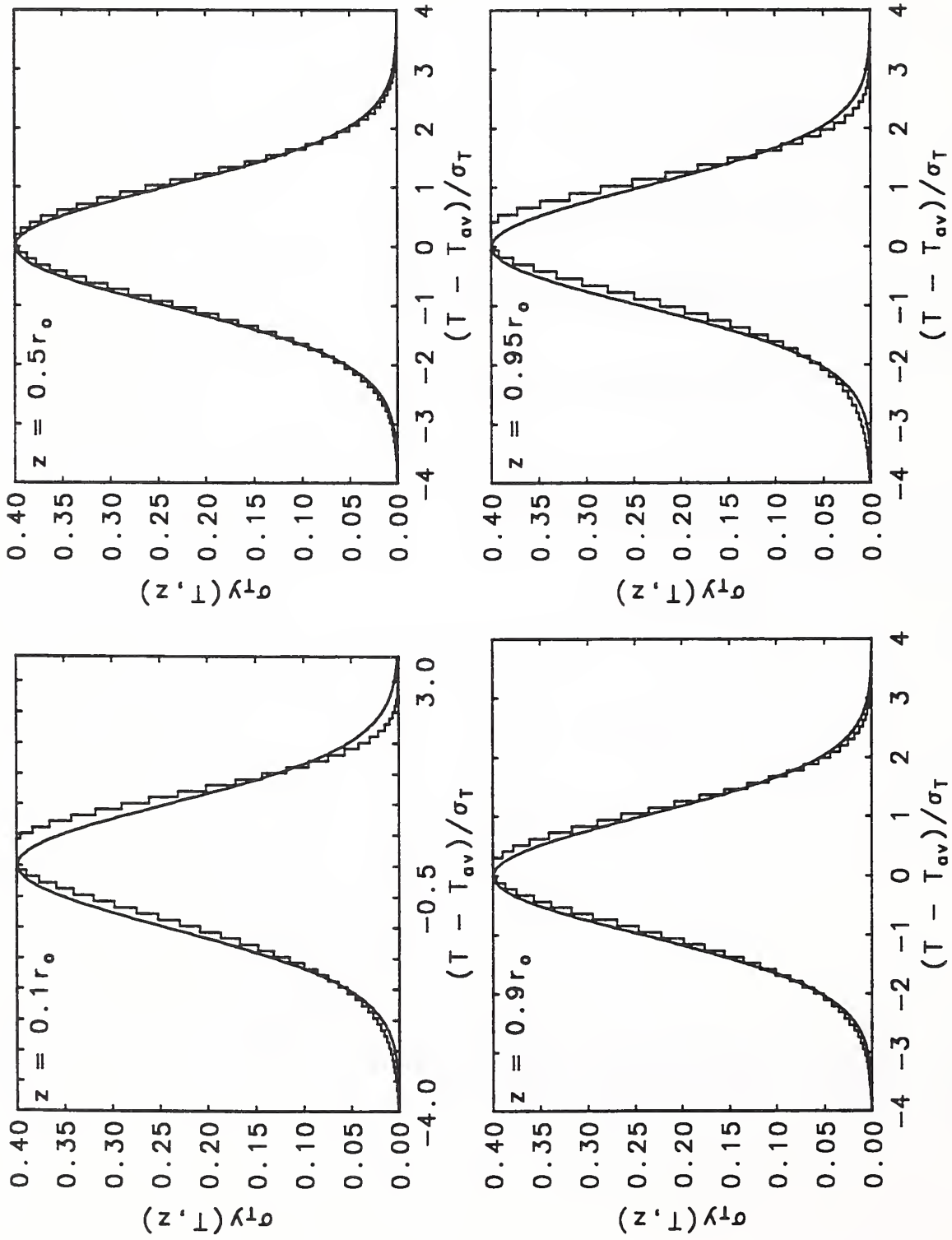


Fig. 17a. Departure of proton energy spectra from a Gaussian distribution. The histograms are results from PTRAND. The curves represent a Gaussian distribution with zero mean and unit standard deviation. The results pertain to an incident 160-MeV beam. Spectra at depths from 10% to 95% of r_0 .

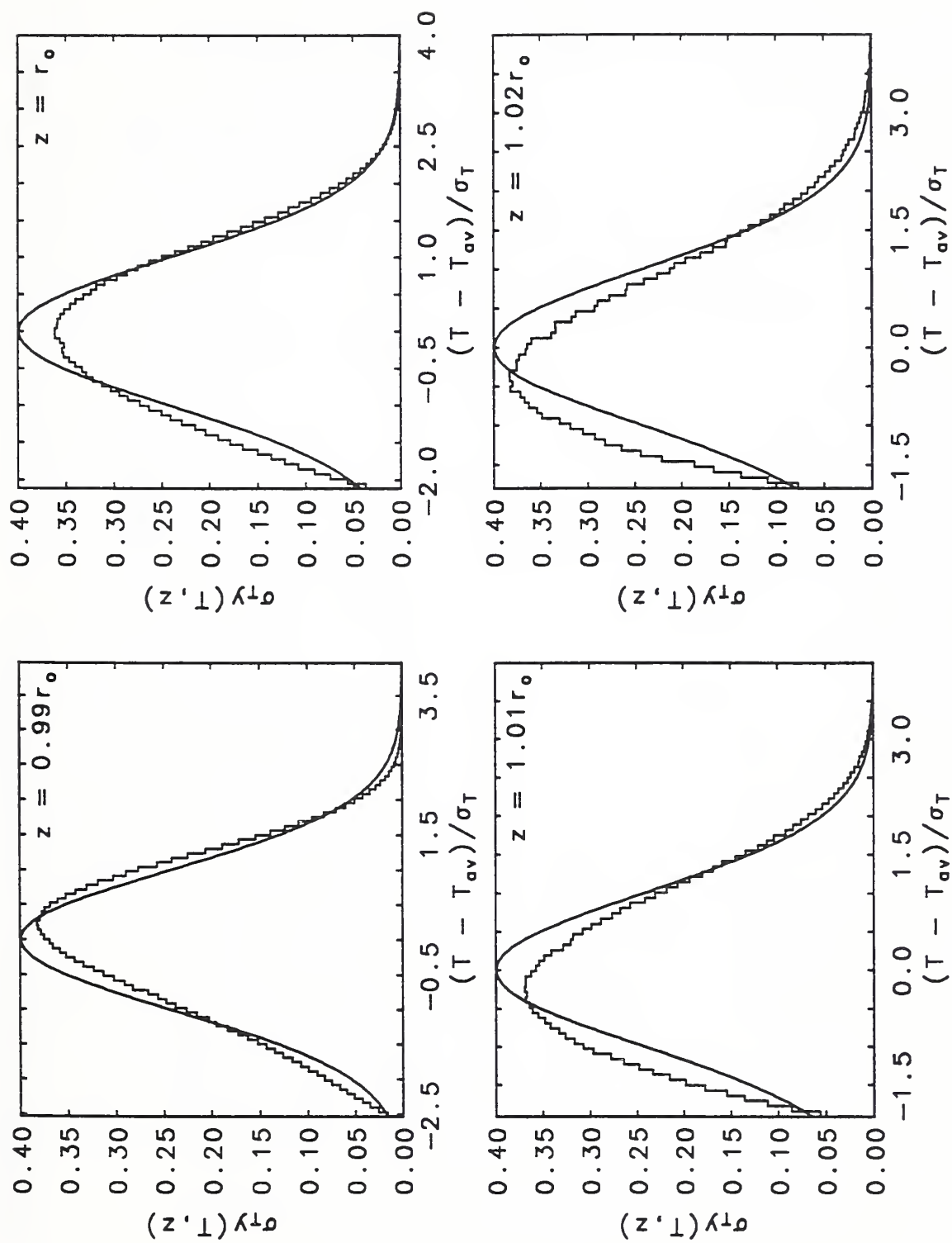


Fig. 17b. Departure of proton energy spectra from a Gaussian distribution. The histograms are results from PTRAN1D. The curves represent a Gaussian distribution with zero mean and unit standard deviation. The results pertain to an incident 160-MeV beam. Spectra at depths from 99% to 102% of r_0 .

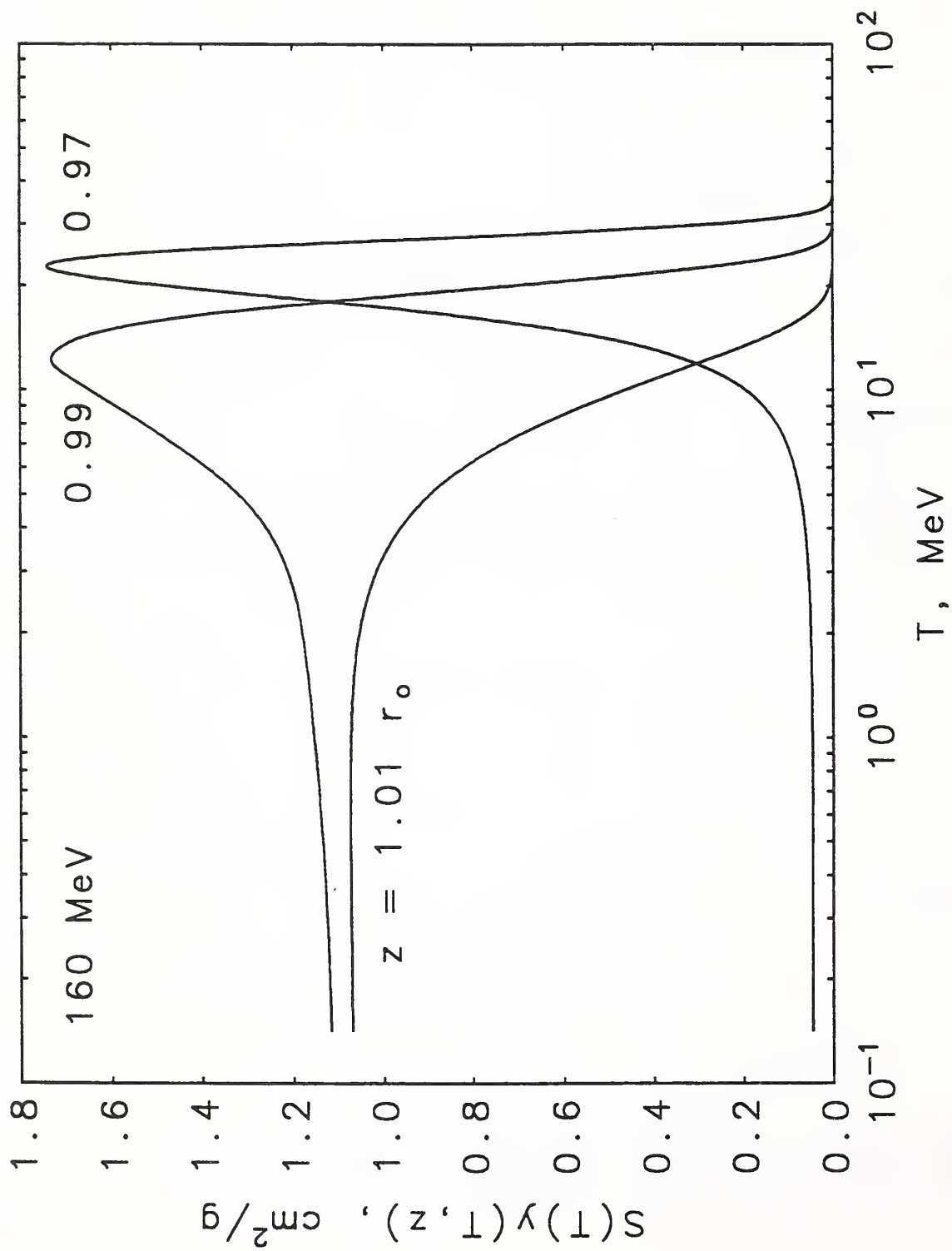


Fig. 18. Proton energy spectrum multiplied by stopping power, $S(T)y(T, z)$, at depths near and beyond the Bragg peak. Results are for an 160-MeV beam.

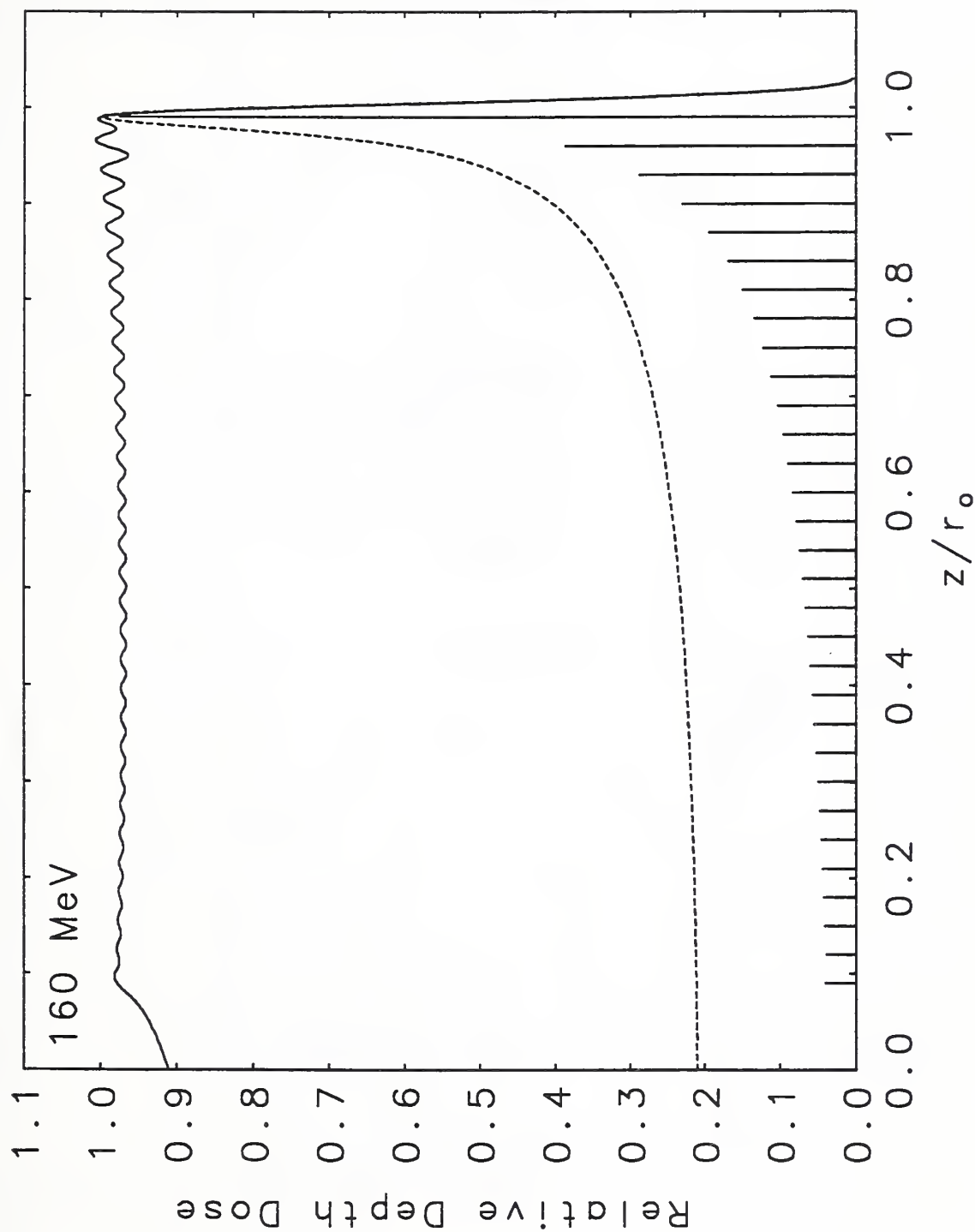


Fig. 19a. Proton energy spectra at various depths in a medium irradiated by a spread-out dose distribution. Comparison of spread-out depth-dose distribution (solid curve) with that for a monoenergetic 160-MeV beam (dotted curve). The vertical lines indicate the positions and intensities of the Bragg peaks contributing to the spread-out beam.

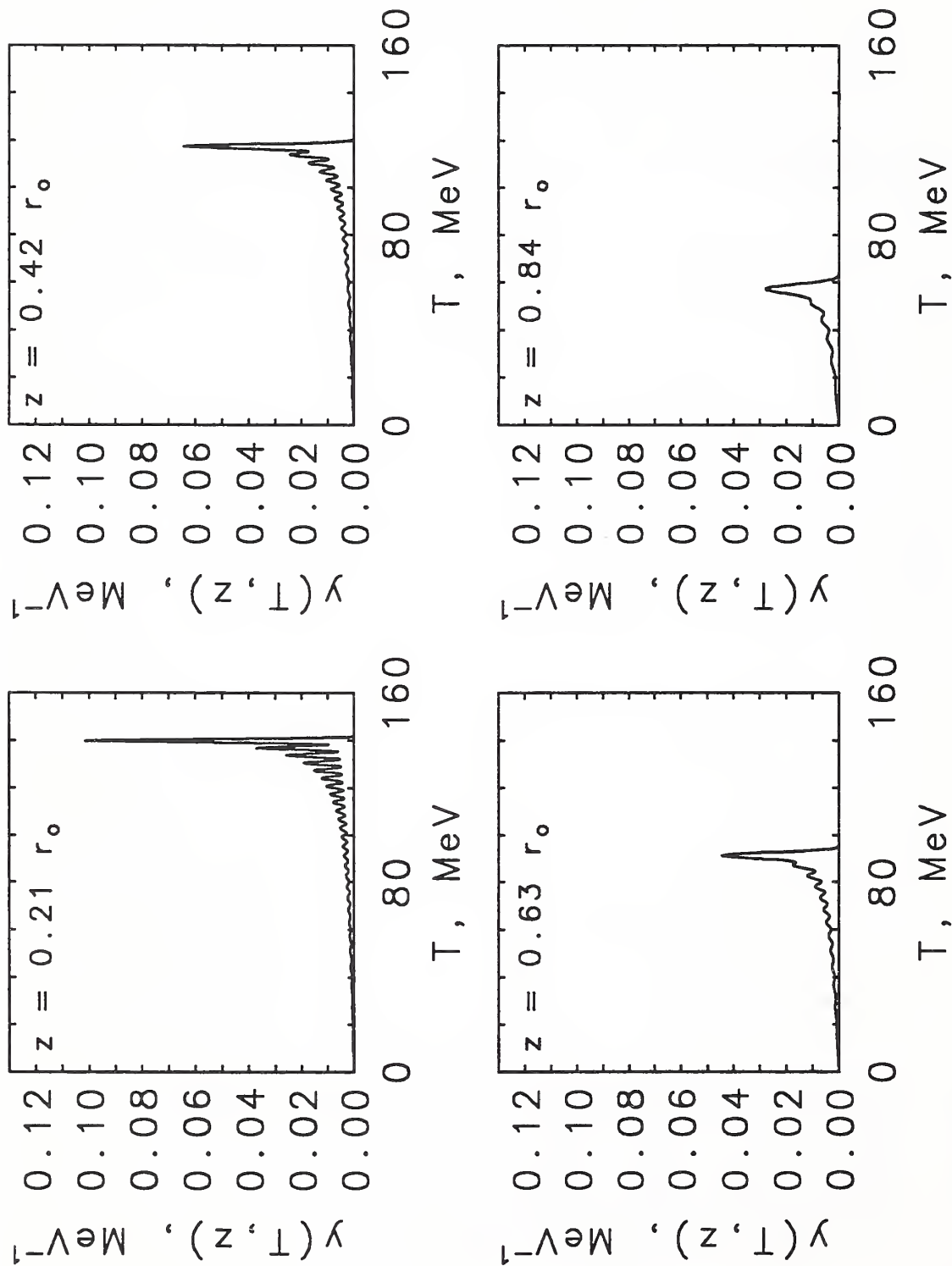


Fig. 19b. Proton energy spectra at various depths in a medium irradiated by a spread-out dose distribution. Energy spectra for spread-out beam.

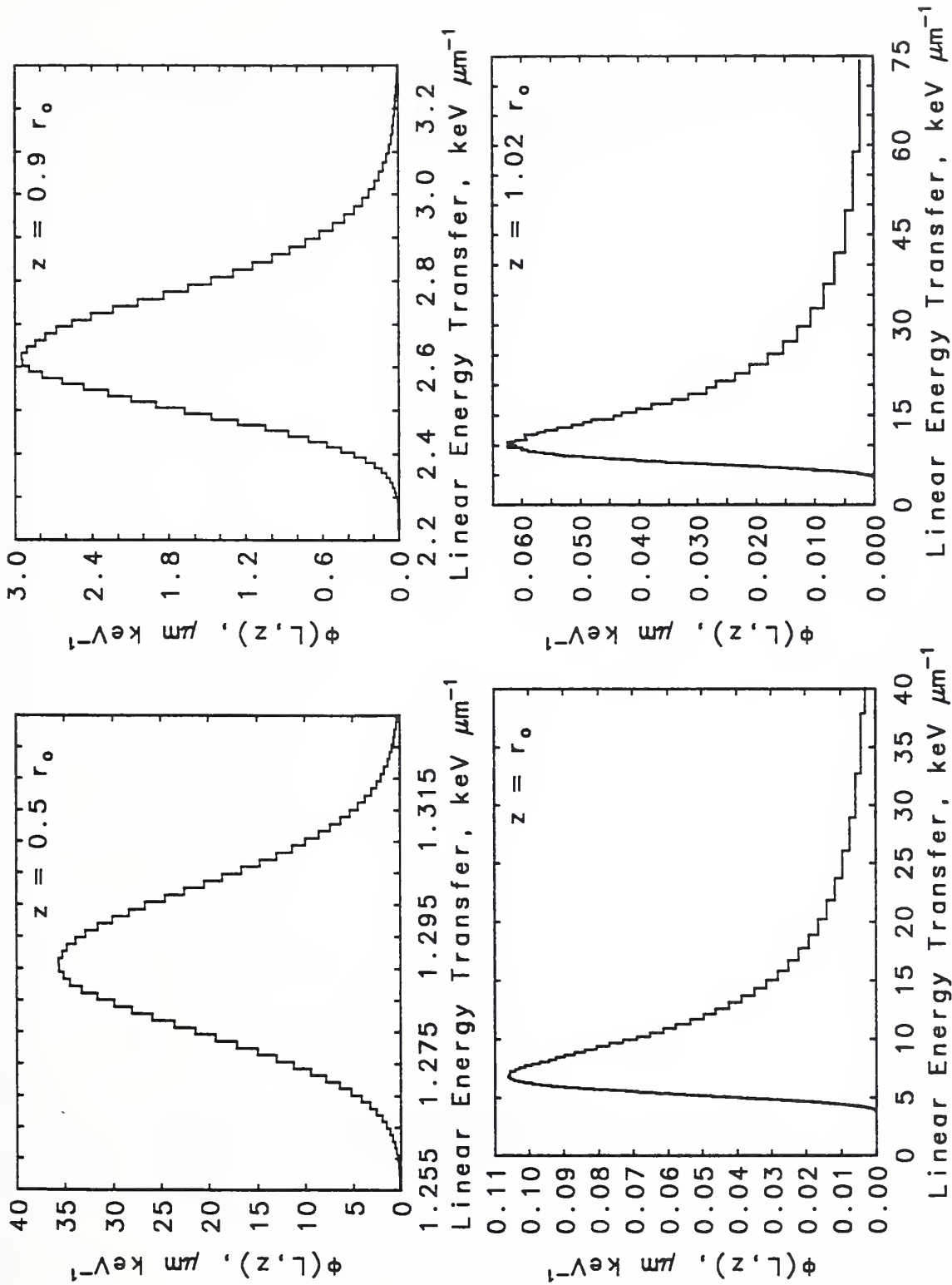


Fig. 20. LET distributions for primary protons, for a 160-MeV beam. The quantity $\phi(L, z)dL$ represents the fraction of the energy deposited at depth z by primary protons that is contributed by protons with LET values between L and $L + dL$.

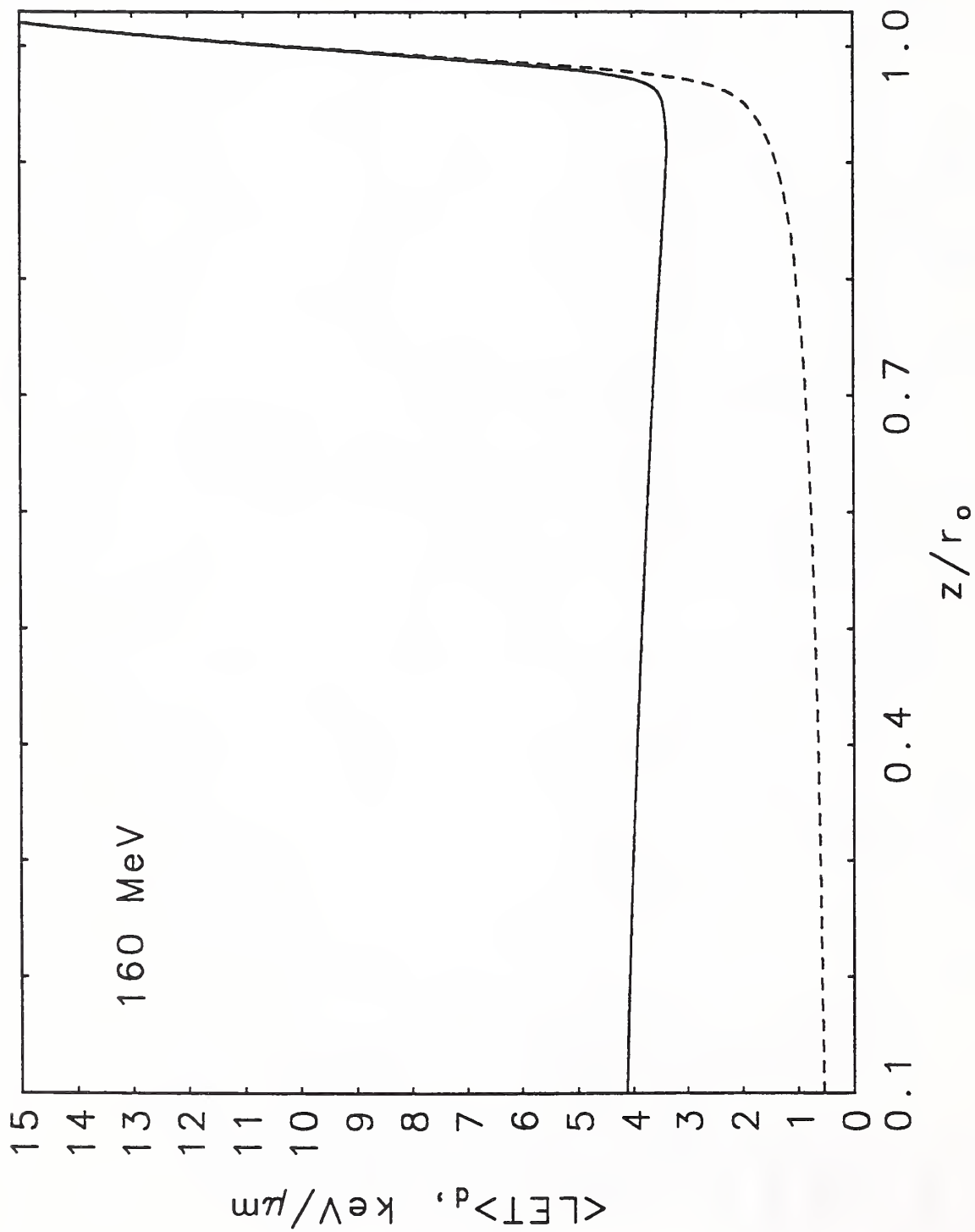


Fig. 21a. Dose-averaged LET as function of depth. The dotted curve takes into account only primary protons. The solid curve in addition takes into account the secondary charged particles from nuclear reactions. This contribution was obtained from a recent calculation by Seltzer (1993). For a proton beam with energy $T_0 = 160 \text{ MeV}$.

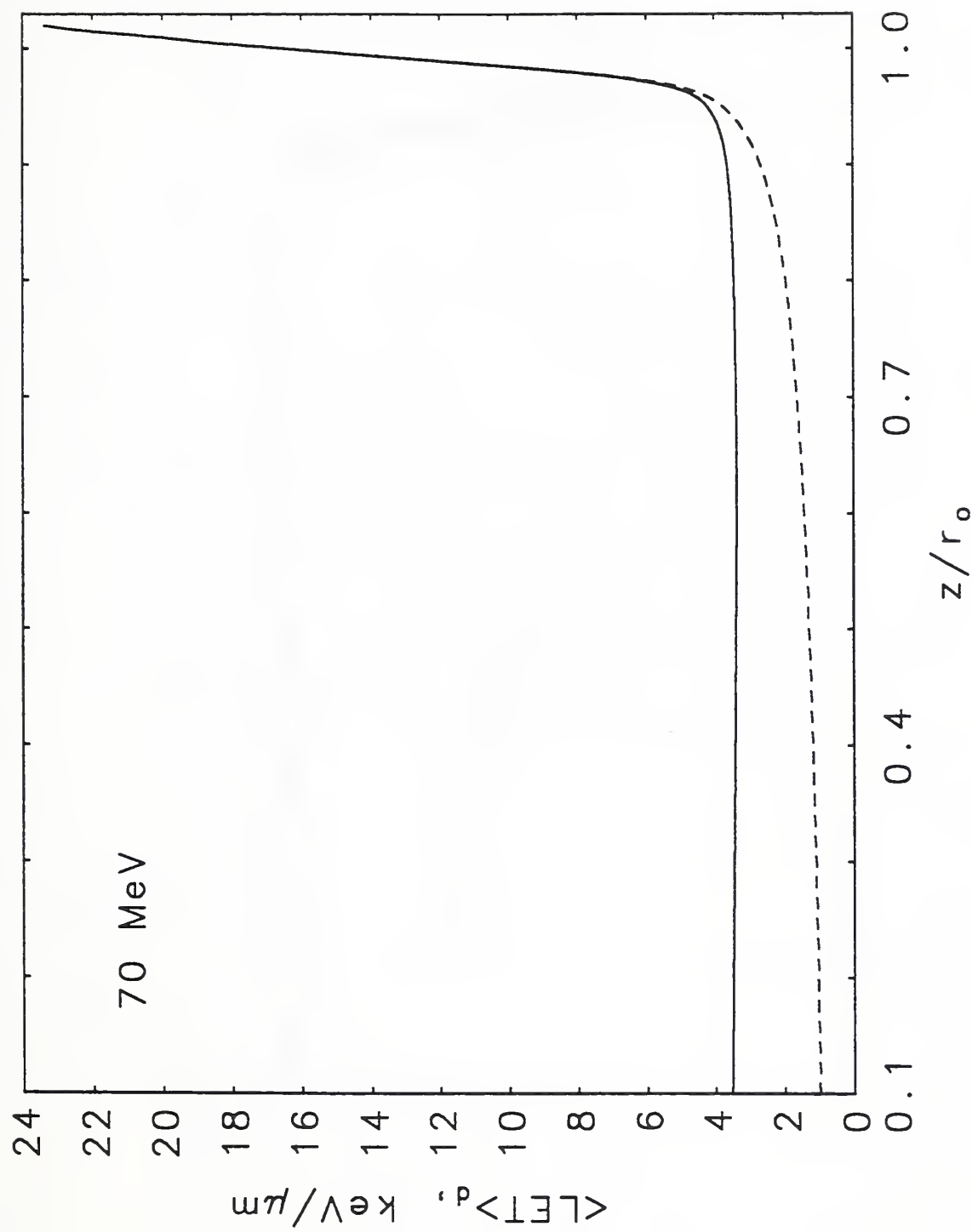


Fig. 21b. Dose-averaged LET as function of depth. The dotted curve takes into account only primary protons. The solid curve in addition takes into account the secondary charged particles from nuclear reactions. This contribution was obtained from a recent calculation by Seltzer (1993). For a proton beam with energy $T_0 = 70$ MeV.

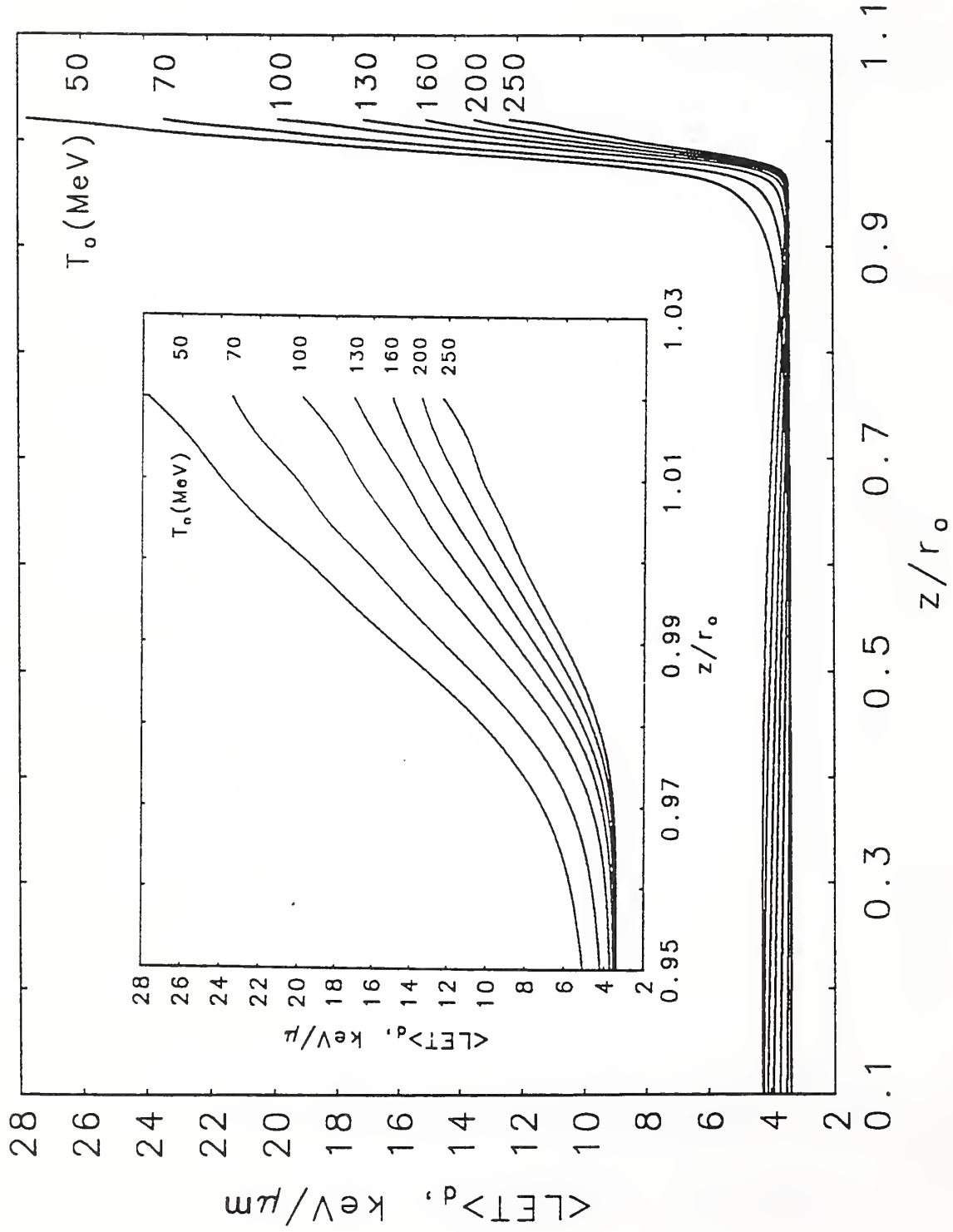


Fig. 22. Dose-averaged LET as function of depth, for monoenergetic proton beams with energy $T_0 = 50, 70, 100, 130, 160, 200$ or 250 MeV. The results take into account the contribution of primary protons, and of secondary charged particles from nuclear reactions. The insert plot shows greater detail in the region of the Bragg peak and beyond.

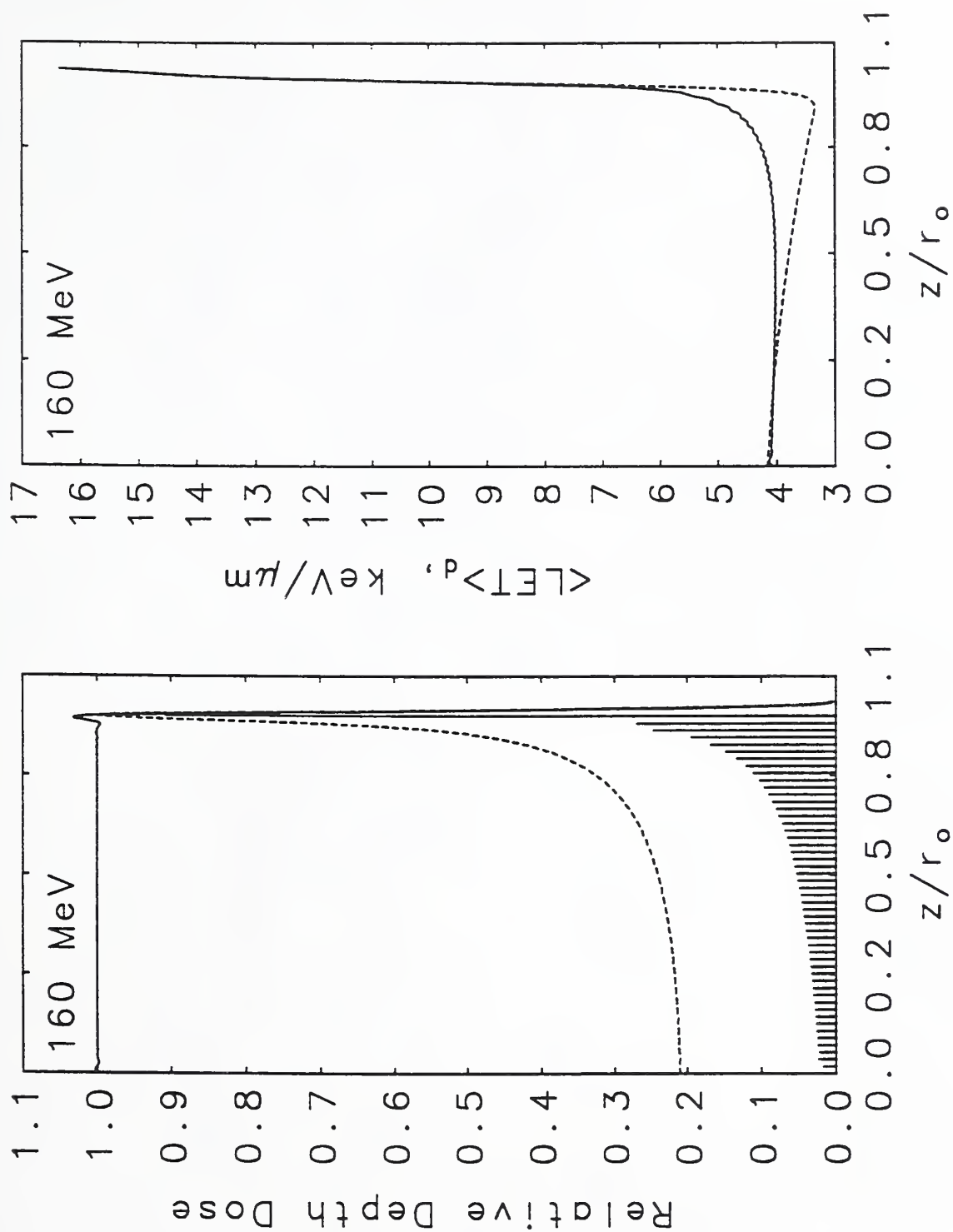


Fig. 23a. Dose-averaged LET as function of depth for spread-out proton beam. Panel on left compares spread-out depth-dose distribution with distribution for monoenergetic beam. Panel on right shows dose-averaged LET vs. z/r_0 for spread-out beam (solid curve) and for monoenergetic beam (dotted curve). Comparison at 160 MeV.

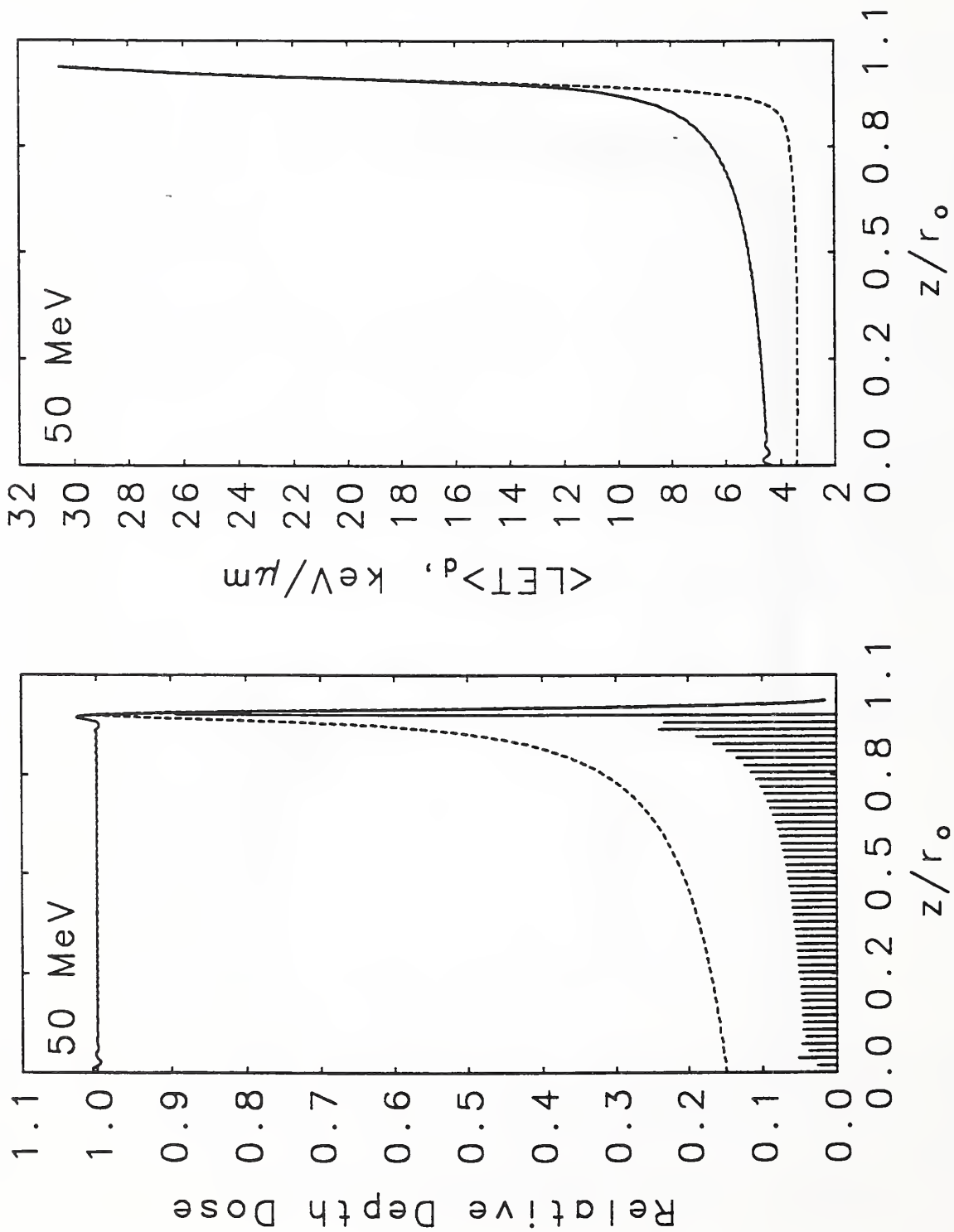


Fig. 23b. Dose-averaged LET as function of depth for spread-out proton beam. Panel on left compares spread-out depth-dose distribution with distribution for monoenergetic beam. Panel on right shows dose-averaged LET vs. z/r_o for spread-out beam (solid curve) and for monoenergetic beam (dotted curve). Comparison at 50 MeV.

